DIRECT NUMERICAL SIMULATION OF STRESS STATES IN WHITE MATTER VIA A TRIPHASIC CONTINUUM MODEL OF 3D AXONS TETHERED TO GLIA

By ROBERT DE SIMONE

A thesis submitted to the

School of Graduate Studies

Rutgers, The State University of New Jersey

In partial fulfillment of requirements

For the degree of

Master of Science

Graduate Program in Mechanical and Aerospace Engineering

Written under the direction of

Assimina A. Pelegri, PhD

And approved by

_____

_____

_____

New Brunswick, New Jersey

January, 2019

ABSTRACT OF THE THESIS

Direct Numerical Simulation of Stress States in White Matter Via a Triphasic Continuum Model of 3D Axons Tethered to Glia

by ROBERT DE SIMONE

Thesis Director:

Assimina A. Pelegri, PhD

Three finite element sub-models were generated with the intent of studying stress propagation in axons under a uniaxial tensile load. The first sub-model used purely non-affine kinematics, where the axons acted independently from the ECM. The second and third sub-models used two different representations of oligodendrocytes to study how stress distributions in the axons are affected by the addition of glial cells. The two sub-models with oligodendrocytes had higher nominal stresses in the system, but lower peak stresses – indicating that the oligodendrocytes do support axons in the extracellular matrix and distribute stresses across the entire system. All three sub-models showed high stresses in regions with high tortuosity and bending stresses between all inflection points in the axon paths. Bending stresses indicate that the system can suffer from fatigue damage if subjected to repeated tensile and/or compressive loading.

Acknowledgements

I would like to thank my advisor, Professor Assimina A. Pelegri, for her support and encouragement throughout the entirety of my studies at the department of mechanical and Aerospace Engineering at Rutgers, the State University of New Jersey. I would also like to thank the entire group of students in the Advanced Materials and Structures Lab for their help and during my time with them. I would like to thank all my co-workers and supervisors at Marotta Controls, Inc. for their patience and mentorship through my graduate studies. I would like to especially thank my family for their unconditional love and support, as I would not have been able to accomplish anything without them.

Table of Contents

List of Tables

List of Illustrations

List of Acronyms and Symbols

TBI	Traumatic Brain Injury
FE	Finite Element
FEA	Finite Element Analysis
FEM	Finite Element Model
ECM	Extracellular Matrix
RVE	Representative Volume Element
μ	Shear Modulus
α	Nonlinear Parameter
D	Compressibility Factor

1.0 Chapter 1: Introduction

Traumatic brain injury (TBI) is one of the most discussed and researched topics in the 21st century. In recent years, the number of TBI diagnoses has increased, but efforts led to accurately predict and measure the magnitude of cerebral injury has proven to be a significant challenge. The corpus callosum has been identified as a critical region for TBI with axonal injury being the proximal cause [9, 19, 25-27]. TBI is often associated with rapid accelerations and decelerations of the brain in the skull cavity secondary to an external stimulus [28, 29, 30]. Diagnosing TBI relies on studying living subjects but measuring the magnitude of the TBI must occur post-mortem. Advancements in technology have brought in new ways to examine TBI post-mortem, but efforts led to accurately predict the extent in live-specimens has proven to be a great challenge [31, 32]. Accurately predicting tissue properties in living tissue also brings great difficulty, as mechanical properties of living tissue differs greatly when studied pre- and post-mortem [11].

Axonal damage has been identified as the leading cause of TBI, with excessive tensile strain postulated as the underlying mechanic [1, 2, 6, 8, 9, 24]. Under routine movements, the spinal cord regularly experiences “large” strains. Studies have shown that the spinal cord tissue can experience 6-10% strain under normal movement. Tests have been performed to measure mechanical properties of axons and white matter in porcine, guinea pig, and bovine specimens due to the equivalence to human tissue [2,11].

Accurately predicting the magnitude of TBI in living test subjects brings great difficulty. Mathematical models have been developed to create basic macro-scale

representations of the human brain, but they often lack the accuracy obtained at the microscale [3]. The adoption of finite element analysis in the field of engineering has given engineers the ability to predict and understand the mechanical response that a representative model yields to an external perturbation [36]. FEA requires the user to provide accurate material properties, a sufficient mesh, real-life representative loads, and proper boundary conditions to achieve accurate results. The finite element Method has been used multiple times in attempt to model the axon-matrix interface at a micro-scale. Multiple efforts have been made to create a finite element model of the human brain stem to better understand micro-scale mechanics of TBI with varying success [1, 3, 4].

In beginning a finite element analysis, a representative geometry of the system must first be created. A microscopic-scale representation of axons and the surrounding grey matter must follow geometric constrains dictated by a human brainstem. Axons modeled using the finite element (FE) method must have the same dimensions and undulation constraints so that the microscopic-scale model will accurately represent axons in a living subject. Axon representations must have dimensions that are consistent with a real-life system [13]. Axons also do not run in straight paths through the extracellular matrix, but rather follow a tortuous path. Each axon has an independent, and seemingly random, tortuous path that must be randomly generated and repeated to create an accurate FE model [12]. The corpus callosum contains axons that follow an ordered path, but they are still randomly undulated as they propagate through the ECM [34, 35].

Material properties are the simplest, yet most significant part of any analysis. The proper material properties coupled with the assigned material models will determine how closely the analysis will be representative of the actual system. Multiple studies have been

conducted on finding proper material properties and models for both the axons and ECM [1- 3, 5- 6, 9-10, 12, 16-18]. The Ogden theory of hyperelasticity is the most agreed upon model that sufficiently represents the brain matter's response to an external load.

To supplement proper material properties and models, appropriate interaction properties must be applied for between the axons and ECM. Studies previously performed treated the axon-ECM interaction as a composite where each axon is embedded into the ECM [1,3-4]. Treating the brainstem as a composite has its merits in simplifying the FE model, but if accurate stresses are to be found in the axons, a different method must be used. Axons are recorded to follow affine and non-affine kinematics through the ECM, where axonal motion is either fully independent of the ECM or is completely dictated by ECM movement [12].

An effort to create a representative volume element (RVE) of the corpus callosum was initiated by Yi Pan at Rutgers University [1]. Pan used a model that represented axons of an equal diameter propagating through the ECM with two-dimensional undulation. The model, created with a Python script, was analyzed in Abaqus 6.14 and subsequently used in an inverse FEA simulation. The inverse FEA method was used to match the FE model's results to experimental test data. the FE model data was then used to create a composite with properties that matched tensile test data. The embedded element method was used to bond the axons to the ECM. The model was run under a prescribed set of boundary conditions with a 20% strain applied to the RVE [7]. The Ogden theory of hyperelasticity was used for both the axon models and the ECM.

A study by Yousefsani et al. describes another effort performed to create an FE model of the corpus callosum [4]. Yousefsani et al. used a model that incorporated axons

of varying diameters passing through the ECM. The diametral distribution of the axons was derived from experimental data [14]. The embedded element technique in Abaqus 6.14 was also used to bind the axons to the ECM in this FE model. While this study was able to implement axons of varying diameters into the model, the axons did not have any undulation applied. The model also applied a transverse strain normal to the system rather than a uniaxial tension. This model focused on the transverse response of the brain white matter rather than the uniaxial tension seen in Pan's model.

A third study conducted by Karami et al. used a fiber-reinforced composite to model the axon and its surrounding ECM's response to an outside disturbance [3]. This study included a single undulated axon surrounded by ECM material. The applied geometry was designed with repeatability in mind to allow for scaling to a larger scale model. Like the other studies, the embedded element technique was used to bind the axon to the ECM. The axons represented in this study followed a predetermined sinusoidal path. Karami et al. applied three load cases which included tension, bending, and shear stresses applied.

In the FE model, Stresses measured in axons and ECM can vary greatly depending on the material properties and boundary conditions applied. All three models mentioned use the modified Ogden theory of hyperelasticity with the application of pure affine kinematics. The decision to use affine or non-affine kinematics will affect the model's response to an external disturbance. An experiment by Bain et al. measured how changes in axon tortuosity will affect how each axon interacts with the ECM and effectively transitions from affine to non-affine kinematics [12]. The three referenced models used affine kinematics, where the axons are fully tied to the ECM. As axon tortuosity increases

and decreases, the constraints tying the axons to the ECM change as well. A composite model using the embedded element technique will allow for stresses and strains to be measured at a macroscopic scale as long as the composite model is specifically set up to match existing test data. The embedded element technique is a computationally inexpensive method of modeling composites, but it lacks the accuracy needed to measure stress propagation at the axon level [15, 33].

Glial cells are often thought of as the "glue" that hold the axons together. More specifically, oligodendrocytes bond multiple axons to each other and create a myelin sheath that insulates and supports axons in the brainstem. The glial cells create a scaffold that supports the axons and can potentially bind 80 axons to a single oligodendrocyte [20, 21]. The previous models did not compare the extent to which axons are supported by oligodendrocytes.

This paper describes a new effort undertaken to model the stresses experienced by an axon under a tensile load. Pan's finite element model was used as a baseline, with modifications applied to allow for piece-part modeling of the axons and ECM. The use of the embedded element technique was replaced by boundary conditions that implement non-affine kinematics. Like the other studies, the Ogden theory of hyperelasticity was used for both the axons and ECM. Pan's existing mesh was sufficiently refined so that stresses can be accurately measured as a uniaxial tensile load is applied to the FE model. The analysis consisted of three loading conditions: a non-affine condition with frictionless contact applied between components, a non-affine model with multiple oligodendrocytes connecting to multiple axons, and a non-affine model with a single oligodendrocyte connecting to all axons simultaneously. This paper describes the process used to develop a

functioning FE model and the results that the model was able to generate under the prescribed loading conditions.

2.0 Chapter 2: Previous Work

This current effort to create a finite element model of the corpus callosum is influenced by works done by Pan et al. [1], Karami et al. [3], and Yousefsani et al. [4]. The strengths and weaknesses of each model are described in the forthcoming sections.

2.1 Underlying Theory

Axon undulation follows a strict set of parameters as they propagate along the length of the brainstem [12]. When modeling the corpus callosum, the axons loosely follow an ordered but random sinusoidal wave pattern as they propagate through the extracellular matrix (ECM). Recording accurate stresses in the finite element model fully depends on how accurately the real-life system is able to be modeled. Axon undulation will play a significant role in determining how the forces are distributed along the length of an axon.

Affine and non-affine kinematics describe how the axons interact with each other, the surrounding ECM, and glial cell network. With affine kinematics, the axons are fully tied to the surrounding ECM – therefore the axons will deform in the same manner that the ECM does. A graphical representation of an affine model under tensile load can be seen in **Figure 1(A)**. In a non-affine kinematic model, the axons are not coupled to their surrounding ECM, but they are still able to interact with each other and the ECM. As seen in **Figure 1(B)**, the length of the undulated axon increases by the same distance that the environment was, but the total path length of the axon stayed constant.

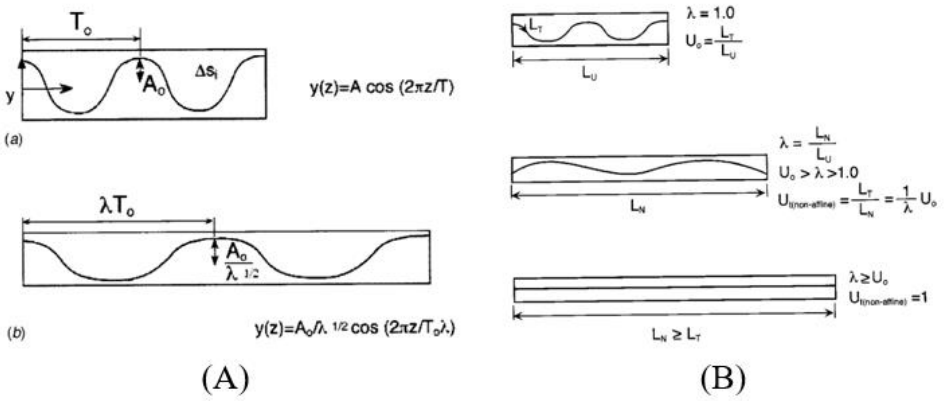

Figure 1: (A) Graphical representation of an axon and surrounding ECM using affine kinematics [12]. (B) Model describing the non-affine relationship between the axons and ECM [12].

2.2 Randomly Undulated Composite Model (Pan,Pelegri et al.)

In the Pan & Pelegri et al. model (Randomly Undulated Composite Model), each axon followed a random tortuous path. The axons were superimposed into the ECM, where the embedded element technique was used to tie the axons to the surrounding ECM. The axons were effectively fully tied to the ECM, restricting the finite element model to affine kinematics only. The RVE stretched in the z-direction up to 25% Strain. Pan's FE model is shown in **Figure 2**.

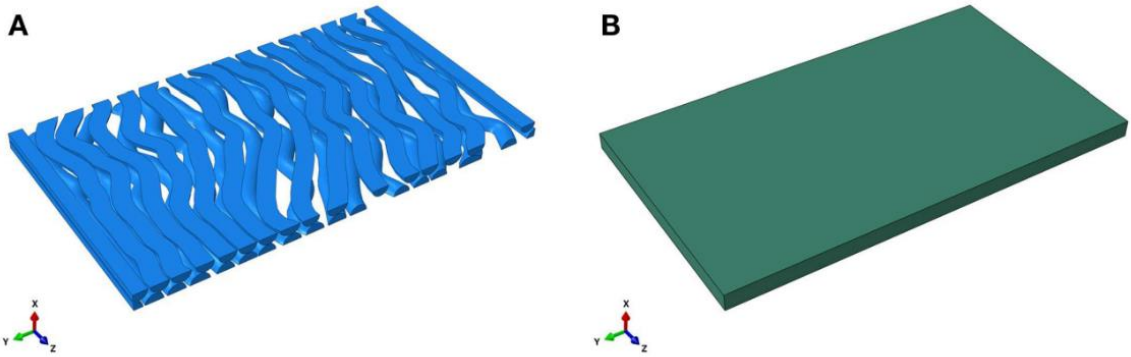

Figure 2: Pan's RVE. 33 axons modeled - each with a random undulation.

While Pan successfully created a model with geometry representative of a real-life system, the model had some shortcomings. The FE model only used affine kinematics due to the use of the embedded element technique. The generated mesh was also too coarse to yield accurate stresses in the axons. The FE model has many instances where high stress gradients occurred across single elements. The model has multiple regions where concentrated stresses occur at regions with little mesh refinement. A much finer mesh is needed for an accurate representation of the stress state in the model. **Figure 3** shows examples of the point stresses and poor stress distributions.

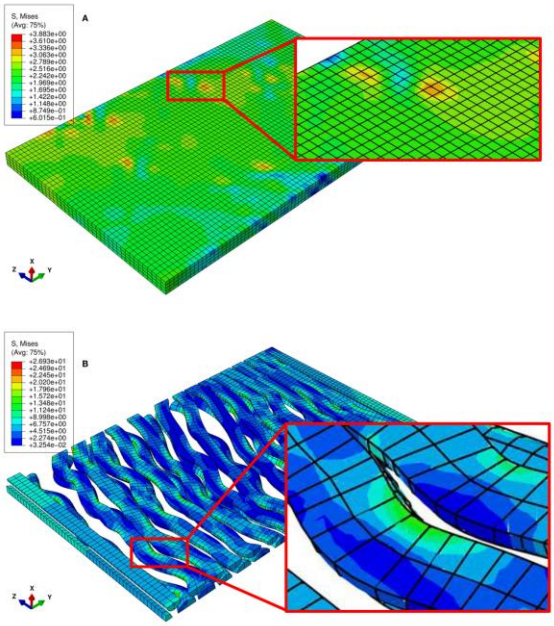

Figure 3: Results from Pan's model [1]. Large stress gradients and localized stresses can be seen across single elements due to the mesh coarseness.

2.3 Single Undulated Model (Karami et al.)

Karami et al. presented a model that represented a single axon with undulation representative of conditions in the corpus callosum. The model was specifically designed to be repeatable, with a full axon in the middle, and four quarters at each edge of the model

(**Figure 4**). The FE model undulation was set to a single sinusoidal wave period with the axon and ECM following the same trajectory. The axon and the ECM were both modeled separately, with the ECM having cutouts specifically for the axon. The exact method used to bind the axons to the ECM is not specified.

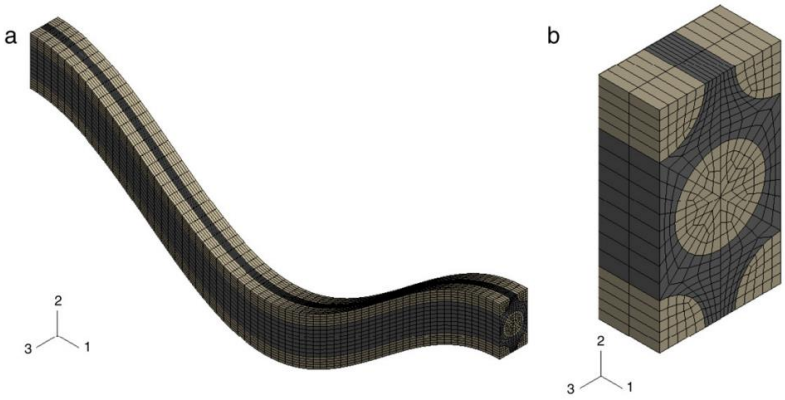

Figure 4: Karami et al.'s finite element model.

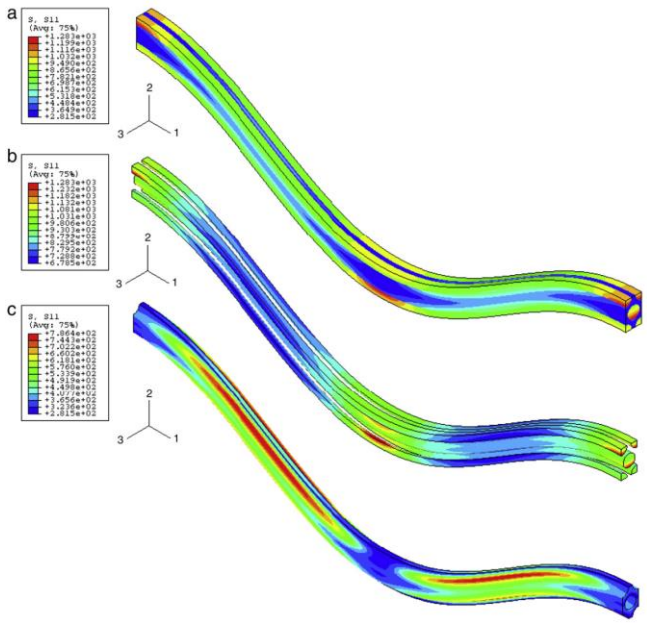

Figure 5: Results from Karami et al.'s analysis [3]

Karami et al.'s model treated the axon-ECM interaction as a composite, where the axon was fully bonded to the ECM. Like Pan's work, Karami et al. was therefore limited

to only using affine kinematics. The FE model represented a single undulated axon and was much more ordered than its real-life counterpart - not considering the randomness associated with axon undulation. **Figure 4** shows the FE model and mesh used. The mesh used was sufficiently fine in the 2-3 plane (using the supplied coordinate system), but in the 1-3 plane, the length of the elements will make it difficult to accurately capture stress of the axon-ECM system as it is subjected to external loading. As seen from the results (**Figure 5**), large stress gradients measured across single elements can be removed with the implementation of a finer mesh.

2.4 Affine Multidiameter Model (Yousefsani et al.)

The model created by Yousefsani et al. is unique to the other two models, as axons of many different diameters were taken into consideration. Based on a statistical distribution of axon diameters in the corpus callosum, several axons were generated with a randomly generated outer diameter [13]. Like the randomness in the diameters, the placement of the axons was also random and not constrained within the bounds of the ECM in the FE model. The embedded element technique was used to bind the axons to the ECM, with stiffness adjustments included to compensate for the volume redundancy. The model composition is shown in **Figure 6**. The mesh used was sufficiently fine, with the results showing evenly distributed continuous stress contours (**Figure 7**).

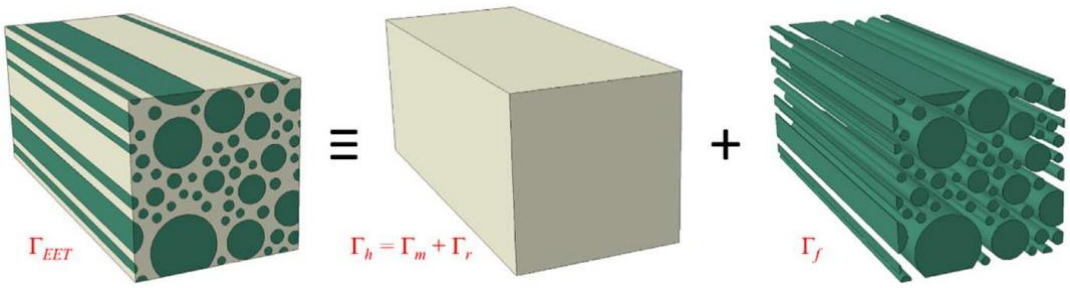

Figure 6: The composition of components in Yousefsani et al.'s Model [4]

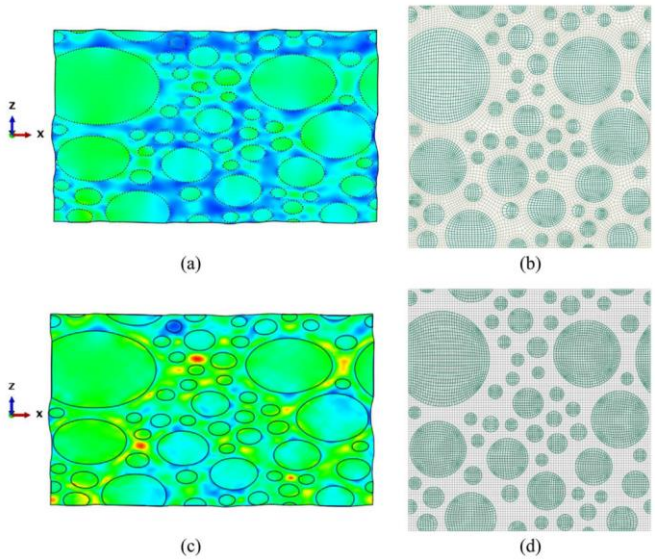

Figure 7: von Mises stress stresses measured in Yousefsani et al.'s FE model [12].

Yousefsani et al.'s model did not focus on randomly generating axon undulation, as the purpose of the FE model was to measure the response to transverse loading (Z-X Plane), so it differed from the other two studies applied. The embedded element technique was used to join the ECM and the axons, allowing only for affine kinematics to be used.

2.5 Commonalities Among the Models

Different philosophies were used to generate all three models, but they all shared similar material properties and material models. All three models treated the axon-ECM

interaction as a viscoelastic composite. The axon and the ECM representations used the Ogden hyperelastic model using coefficients derived from Meaney's research [2].

Treating the axon-ECM interaction as a composite is effective for creating a computationally inexpensive representative volume element, but the stresses seen in individual axons are not able to be accurately represented. The three models are not detailed enough to measure the response that individual axons have to an external load.

The method of generating an RVE should be used after measuring the response that individual axons yield to external mechanical loading. Effectively, all three models created a composite cell and changed the FE model properties until the FE results aligned with real-life experimental data. The use of a composite (and embedded element technique) limits the model to only use affine kinematics and the axons are not allowed to react independently of the ECM. With a composite model, axons are not able to stretch and slide along their channels in the ECM since they are fully bonded to the surrounding matrix.

3.0 Chapter 3: Connecting Oligodendrocytes to Axon-Glial Kinematic Model

After reviewing the three models that were previously used it was decided that improvements could be made to successfully model axonal stress propagation. All three models succeeded in their own way, but each had a major drawback due to treating the axons and ECM as a composite at the macro-scale. This not only limits the models to be working purely with affine kinematics, but it also disregards the axons interacting individually with the ECM as the model is loaded.

It has been proven that axonal failure is the underlying mechanic of traumatic brain injury - understanding how stresses develop in the axons will give more insight to the onset of TBI. The three models did succeed in generating a macro-scale RVE, but they did not succeed in accurately measuring stresses as the axons were subjected to a uniaxial tensile stress.

3.1 A Triphasic Kinematically-Tethered Model

Pan's model was selected to investigate the axonal response to an external load. Pan was able to successfully model axon tortuosity representative of the human Corpus Callosum into a model that can be analyzed using Abaqus 6.14. Slight modifications to Pan's model are described in this section.

Focusing solely on stress propagation in axons, the composite representation was postponed for the current study. In moving away from the composite representation, some constraints could be lifted. First, the volume fraction is not as relevant. Monitoring the stresses generated in the axons in the goal of the study -not matching test data to a composite model. Next, with the interest of making the model less computationally

intensive, the number of axons was reduced from 33 to 10. This was deemed an acceptable batch size for the current effort. Finally, the spacing between the axon rows was increased by 0.5 µm so that a valid mesh could be made (see **Figure 8(C)** and **Figure 8(D)**). The height of the ECM section was effectively increased from 4.0 µm to 4.5 µm. **Figure 8** illustrates the change in ECM width.

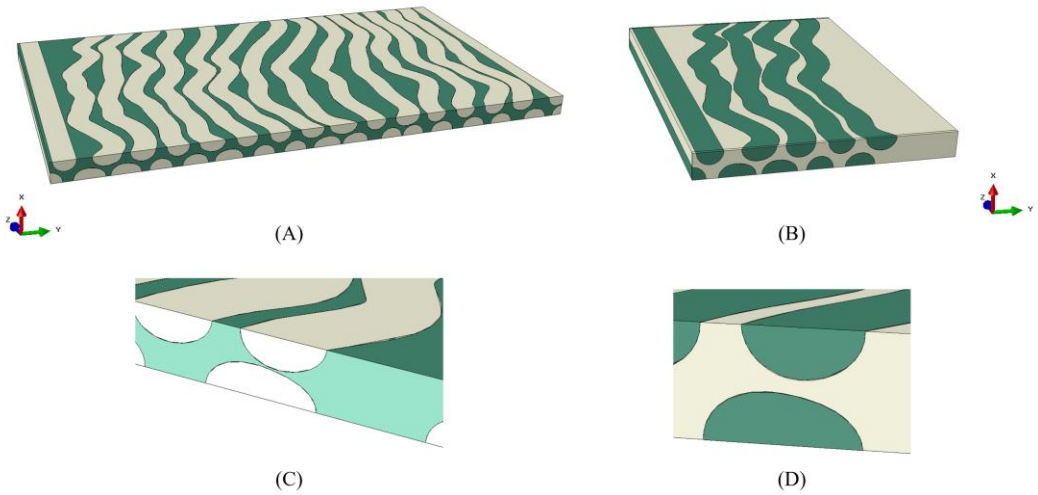

Figure 8: Comparison of the original geometry created by Pan to the new model geometry with slight modifications applied.

During the generation of the mesh, the region in **Figure 8(C)** was unable to create elements of a logical size. The region was assigned elements as small as $1x10^{-6}$ µm and the built-in Abaqus meshing tool was unable to create elements of a sufficient quality. In theory, there is no limit to the size of an element, but the number of elements generated would have made the model too computationally intensive to solve. The accuracy of the solver would have come into question when computing stresses at the order of 10^{-6} or smaller. To make a mesh that yielded elements with sufficient quality (and passing the built-in Abaqus element check function), increasing the gap between the axons was necessary. The previous model was able to get past this limitation with superimposing the

two geometries together and using the embedded element technique. The axon and ECM geometries occupy the same space. The new model not only measures the stresses in the axons under a tensile load, but it also allows for contact between the ECM as the system is subjected to an external load.

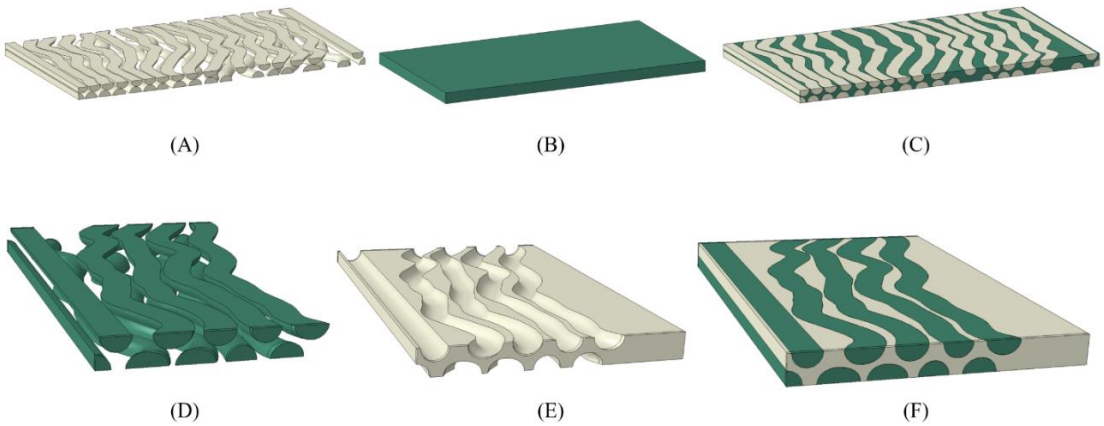

Figure 9: Different modeling methodologies between the models. The embedded element method allows for redundant geometry between axons and ECM (A-C), while the newer model requires the two models to be separate for contact to be applied (D-F).

For contact between the axons and matrix to be applied, the two geometries could no longer use redundant volume conditions. The Abaqus built-in Merge/Cut Instances function in was used to cut the axon paths through the generic ECM geometry [15]. **Figure 9** shows the differences between the two models. In **Figure 9 (D-F)** the axons have channels that are cut based on the axons' tortuous path.

3.2 Material Properties

Based on many studies devoted to characterizing neural tissue, the Ogden Model was chosen to represent the Axons and ECM in the current model [1- 3, 5- 6, 9-10, 12, 16-18]. The Ogden model of hyperelasticity is a very general and versatile model – it is also the

most commonly used model used to represent biological tissue under uniaxial loading. The model versatility allows for neural tissue to be characterized relatively easily and with very little error – assuming the test data from material characterization is sufficient. The Ogden model is expressed in terms of the applied principle stretches [18]. The materials used in this analysis are considered incompressible, resulting in **Equation 1** below. Under uniaxial tension in an incompressible Ogden model, the stresses experienced by the axons and ECM can be measured using $\boldsymbol{\sigma uniax}= \sum_{k=1}^{N} \frac{2\mu_k}{\alpha_k} [\lambda^{\alpha_k} - \left(\frac{1}{\sqrt{\lambda}}\right)^{\alpha_k}]$

Equation 2**.**

$$U = \sum_{i=1}^{N} \frac{2\mu_i}{\alpha_i^2} (\bar{\lambda}_1^{\alpha_i} + \bar{\lambda}_2^{\alpha_i} + \bar{\lambda}_3^{\alpha_i} - 3)$$

Equation 1: Ogden strain energy potential [18].

$$\sigma_{uniax} = \sum_{k=1}^{N} \frac{2\mu_k}{\alpha_k} [\lambda^{\alpha_k} - \left(\frac{1}{\sqrt{\lambda}}\right)^{\alpha_k}]$$

Equation 2: Ogden model in uniaxial loading [18].

The current FE material model uses a first order Ogden model (a more generalized form), therefore allowing N=1. As mentioned in the previous paragraph, strong test data must be used for reference when characterizing with the Ogden model. Fortunately, a significant amount of research has been performed in past studies to create an Ogden hyperelasticity model representative of neural tissue. Under uniaxial tension, $\boldsymbol{\sigma uniax}= \sum_{k=1}^{N} \frac{2\mu_k}{\alpha_k} [\lambda^{\alpha_k} - \left(\frac{1}{\sqrt{\lambda}}\right)^{\alpha_k}]$

Equation 2 can be used to measure tensile stresses in the FE model components. Undulation prevents the axons from experiencing full tension until a threshold strain is reached (dependent on the amount of undulation in the axon). $\sigma uniax = \sum_{k=1}^{N} \frac{2\mu_k}{\alpha_k} [\lambda^{\alpha_k} - \left(\frac{1}{\sqrt{\lambda}}\right)^{\alpha_k}]$

Equation 2 becomes relevant once the axon reaches an undulation of 1.

Three coefficients needed to be used for the axons and ECM: Shear modulus (μ_i), nonlinear parameter (α), and compressibility factor (D). The values for shear modulus and the nonlinear parameter were provided by test data presented in Meaney's research [2]. The shear modulus of the ECM is derived from the shear modulus assigned to the axon, as the axon is three times stiffer than the ECM per Arborgast and Marguile's findings [9]. Therefore, to find the shear modulus of the ECM, the value of the axon shear modulus is divided by a factor of three. To remain consistent with works previously performed, the nonlinear parameter assigned to the axons and ECM are given the same value. The material assignments for the axons and ECM are incompressible and therefore D is set to zero. See **Table 1** for the values used in both the axons and ECM.

Assigned Material Properties for the Finite Element Model

Component	Shear Modulus (Pa)	D (1/Pa)	α
Axon	290.82×10^6	0	6.19
ECM	96.94×10^6	0	6.19

Table 1: Assigned material properties for the axons and ECM in the FE model.

During the generation of the FE model geometry, all components were modeled using micrometers (a value of 1 in the FE model is equal to 10^{-6} meters). The Abaqus solver operates in a unitless environment, so an adjustment had to be made to keep units consistent. The shear modulus has been multiplied by a factor of 10^6 to compensate for modeling in micrometers. Modeling a μm as a unitless value of 1 in the solver could cause unrealistically high stress to be recorded if the material properties are not adjusted accordingly. A pascal is converted into kg/(m·s^2), which equals 10^6 kg/(μm·s^2). All units of length are reported in μm with all material properties adjusted accordingly.

The parameters in **Table 1** for the Ogden model have been provided and used in multiple studies prior to this one, but the stability of the model with the above parameters must be verified. To check the stability, the Ogden hyperelastic model with the above parameters was evaluated in ABAQUS for any potential instabilities. The model stability results can be found below.

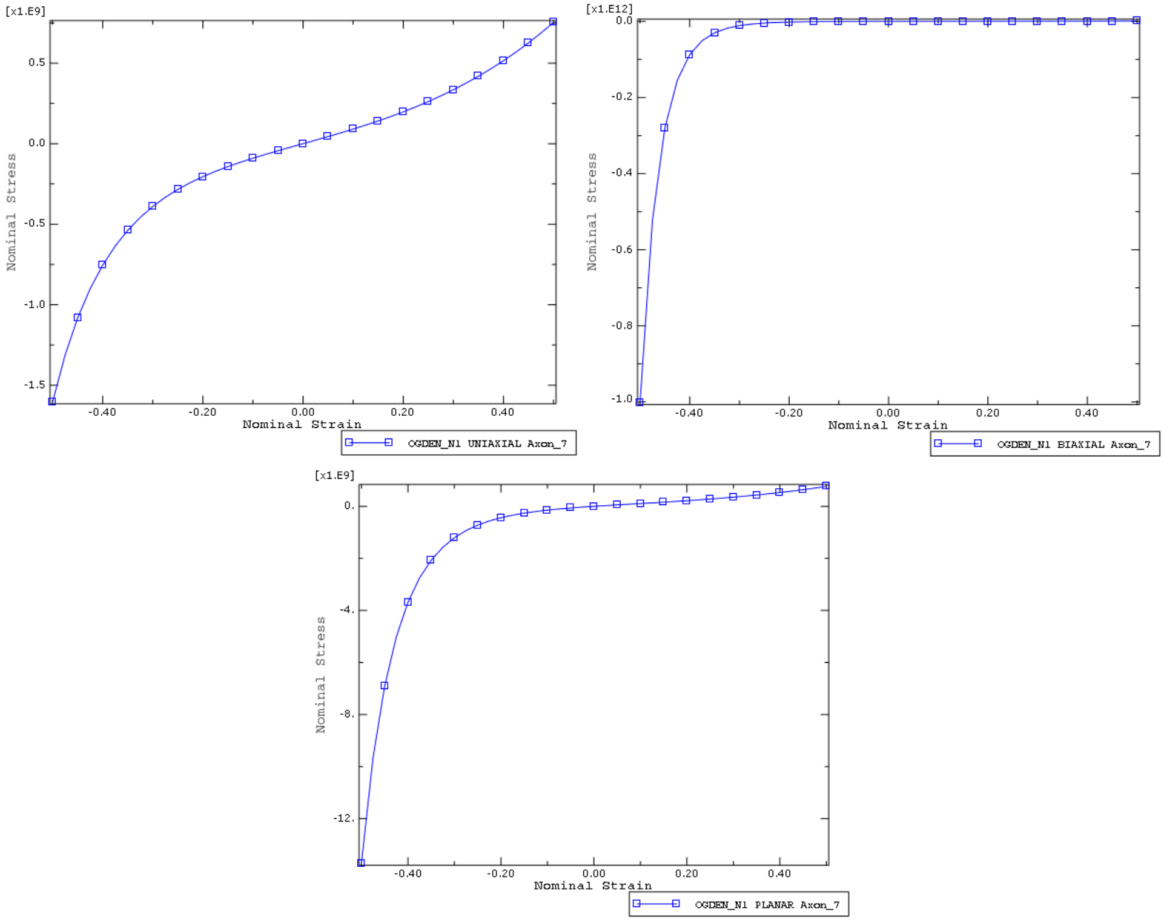

Figure 10: Stability of the axon assigned material properties. The Ogden model of hyperelasticity is stable for the above conditions.

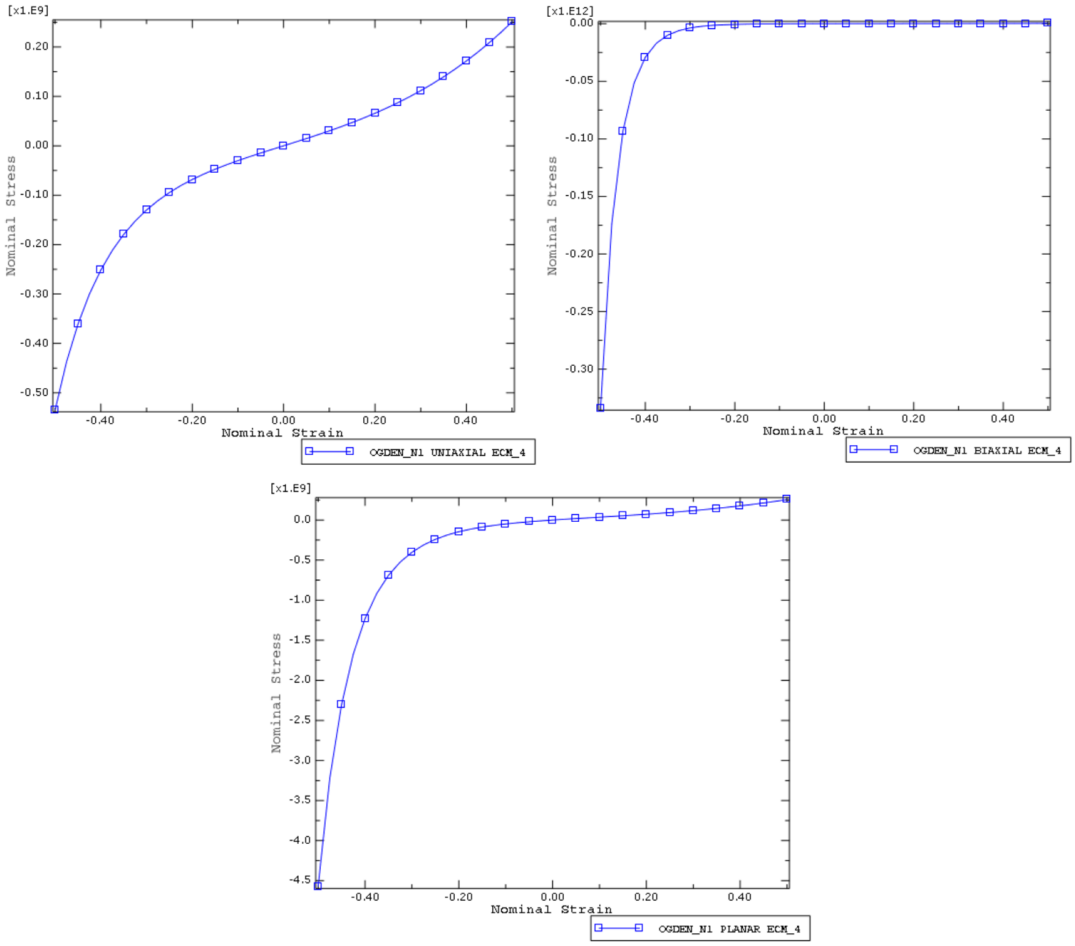

Figure 11: Stability of the ECM assigned material properties. The Ogden model of hyperelasticity is stable for the above conditions.

Figure 10 and **Figure 11** show that the Ogden Model is stable up to a 45% strain applied in uniaxial tension. TBI has been reported to occur anywhere between 10-20% strain, and therefore the FE model will not be subjected to a strain higher than 20%. Based on the stability results, the Ogden model of hyperelasticity can be confidently be used to model the large strains required by the FE model. The graphs for biaxial and planar strain are included to provide confidence in the versatility of the Ogden model when the model is subjected to forces other than uniaxial tension.

After choosing the proper material model and inputting the corresponding material properties, the next step in the analysis is to create a mesh. While the geometry of Pan's original model was able to be repurposed, the mesh needed to be reworked to achieve the goals of the current application. In the previous model, Hex/Hex-Dominated meshing techniques were used globally to create elements in the ECM and axons. Hex meshing techniques are computationally lighter than a tetrahedral due less nodes per element, but the undulated axon geometry combined with the complex contours in the ECM brings risk of generating poor elements.

The use of the embedded element technique in Pan's model allowed for a coarse mesh to be used. The meshed axons were controlled by the number of elements rather than the size of the elements – dividing the axons into 50 segments independent of true axon length. A mesh this course will generate stress fields that can be inaccurate and lead to misleading peak stresses in the FE model. The embedded element technique is very useful for characterizing a composite, but it lacks the accuracy required to monitor stress in each piece part. When the finite element software calculates stress in a component, the stresses at each node are averaged based on the surrounding elements. With an insufficient number of nodes (and therefore elements) a high or low stress region will not have enough elements to accurately calculate the stress experienced. A coarse mesh will cause the average stresses of the surrounding nodes and elements stresses to be poorly sampled [36].

4.0 Chapter 4: The New Model

With minor changes applied to Pan's model so far, the following section details changes deemed as significant to reach the goals of modeling axon stress contours. Three sub-models were generated in the new FE model. First, a sub-model was created to represent a non-affine condition where axons are free to move through the ECM as a uniaxial tension is applied. The three models created previously had the axons either fully tied to the surrounding ECM or taking up the same volume as the ECM as required by the embedded element technique. Next, the second sub-model adds simple representations of oligodendrocytes to the first sub-model. The second sub-model incorporates a supporting scaffold inside of the axon and ECM system. Multiple axons are tied to an array of oligodendrocytes using a spring-dashpot connection. The third sub-model incorporates a single oligodendrocyte connecting to all axons in the model at multiple points. The central oligodendrocyte is bonded to the center and both ends of all ten axons in the model. All three sub-models are subjected to the same uniaxial tensile load. The primary goal of the current study is to monitor how stresses form in the axons as a tensile load is applied. The secondary goal is to record how the addition of oligodendrocytes will affect the stress propagation in the system.

4.1 Sub-Model 1: Non-Affine Model

Geometry from Pan's model was repurposed so that an acceptable mesh could be generated on the axons and ECM. The mesh of the new model was set to be much finer than the original. Instead of using a set number of elements in a given area, a maximum element size was set to each face of the axons. See **Figure 12** for a direct comparison between the mesh density of the previous model and the current. The cylindrical faces of the axons were

set to an element size of 0.045 µm, with the ECM set to a global element size of 0.075 µm. The ECM mesh is coarser than the axon mesh because it is not the focal point of the analysis. The goal of the analysis is to monitor the stresses found in the axons. The ECM mesh can still be used to visualize stress fields in the respective component, but it will not have accurate stresses results.

When generating the mesh, the hexahedral technique was used where possible, but a majority of the axons and ECM required a tetrahedral technique to be used. For eight of the ten axons and ECM, a tetrahedral technique was used to create the mesh. The two axons that followed a straight path were able to be meshed with hexahedral elements.

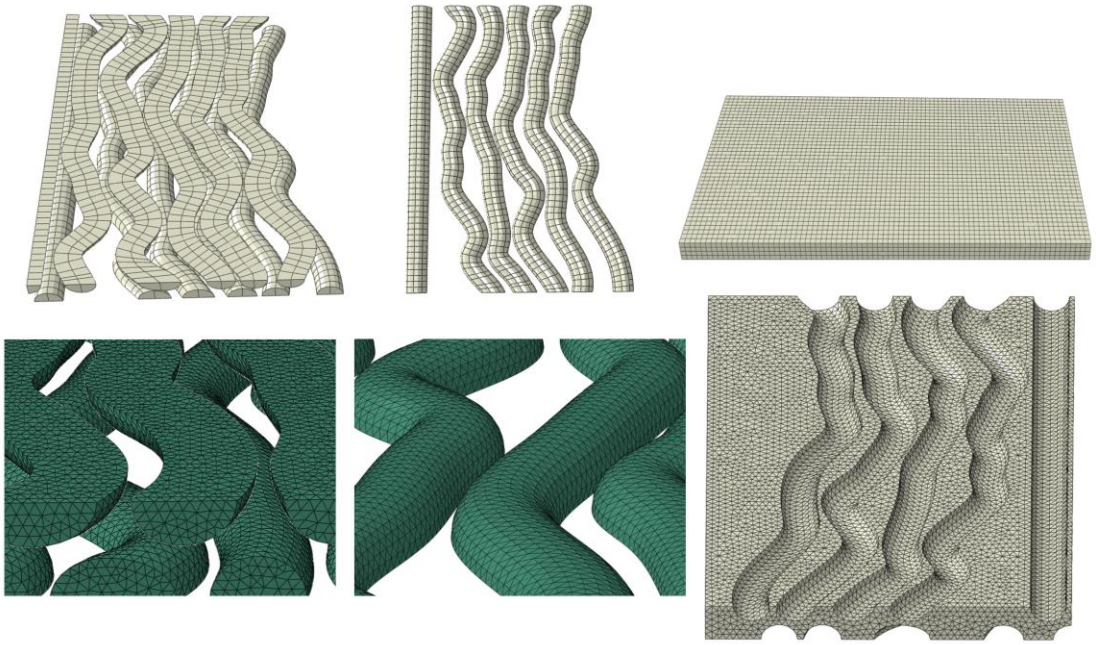

Figure 12: Side-by-side comparison used in the previous model and the mesh generated for the current model.

In total, the new finite element mesh consisted of 79,420 nodes with 320,490 elements. 313,935 elements were Tetrahedral of type C3D4H, 5520 hexahedral elements of type C3D8H, and 1035 wedge elements of C3D6H were generated on the model geometries.

All elements required a linear hybrid formulation due to the hyperelastic material assignment.

Using linear elements brings a high risk of generating abnormally high friction values with the contact between two cylindrical faces. The linear element geometry along with the curved surface that the elements are used to approximate will create a face with non-continuous geometry. Normally, quadratic elements would have to be used (and therefore making the model much more computationally intensive), but Abaqus has a tool that is used to smooth out discontinuous surfaces. The Abaqus surface smoothing function will replace discontinuous transitions between two first-order element faces using parabolic curves [15]. A diagram of this operation is shown in **Figure 13**. The surface smoothing function will allow for the axons to slide along the ECM face without any false frictional values. **Figure 14** gives an example of a linear axon face in contact with a linear ECM face. Note here where the mesh elements overlap, and sharp edges contact the flat element faces.

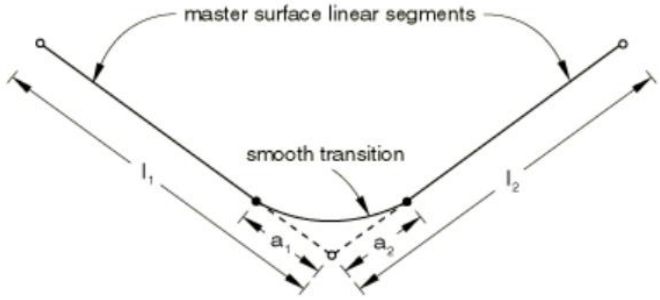

Figure 13: Surface smoothing function between two linear element faces [15].

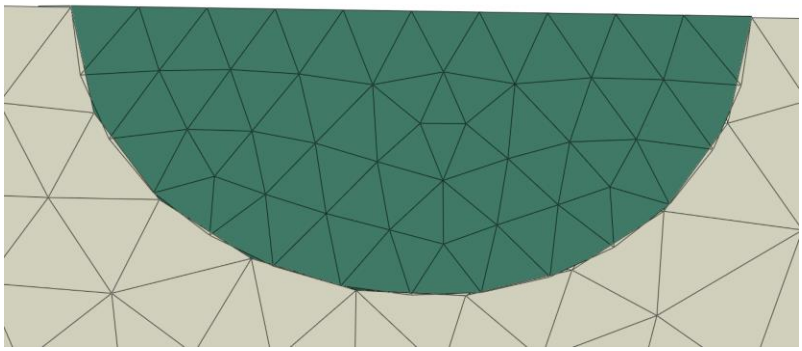

Figure 14: Discontinuous element faces between the axon and ECM models.

Once the material properties were specified and the mesh was created, the contact conditions were the next features to be added to the model. The interaction between the axons and the ECM were identified to be frictionless in the tangential direction, with a "Hard" contact in the normal direction. The specified contact pairs can be seen in **Figure 15**. Abaqus requires a "Master" (red) surface and "Slave" (purple) surface to be called out for each contact pair. As described in the Abaqus documentation, the master surface controls the motion of the slave surface. The goal of this analysis is to study the axonal interaction to external loading, so the ECM was specified as the master surface and the Axon was set as the slave surface.

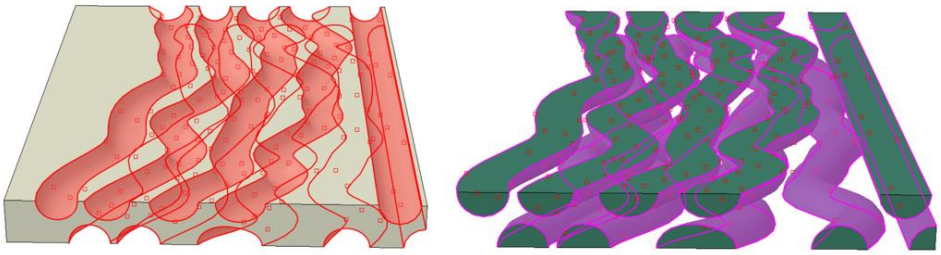

Figure 15:Master surface assignments in the axon-ECM interaction (Left, Red), and slave surface assignments in the axon-ECM interaction (Right, Purple)

In preparation for applying a uniaxial tensile load to the axons and ECM in the finite element model, two constraints were applied to the existing geometry. The axon and ECM faces on the X-Y plane (coordinate system included in Figure 16) at the fore and aft end of the assembly were both coupled to a reference point at the center of each end. Each node on the highlighted assembly face was coupled to the remote point using a kinematic coupling condition. The kinematic coupling condition effectively ties all degrees of freedom to the reference point. **Figure 16** illustrates the coupling constraints in detail.

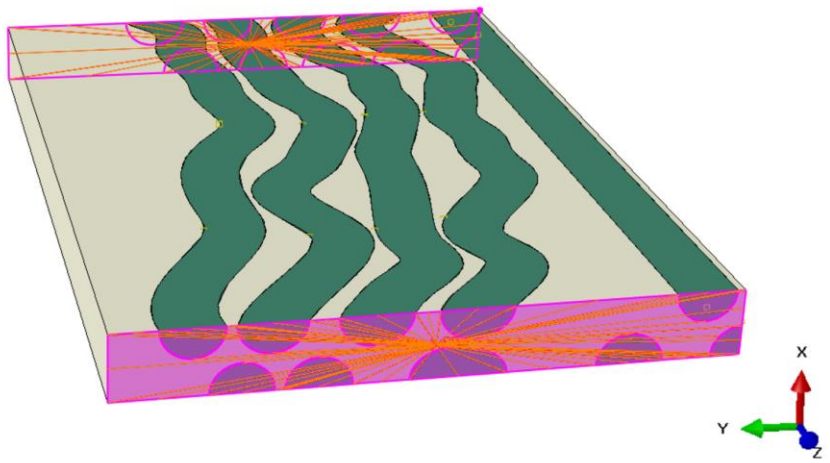

Figure 16: Remote point kinematic coupling to each end of the finite element model.

The boundary conditions applied to the finite element model consisted of symmetry along the Y-Z plane and two displacement boundary conditions. The symmetry boundary condition is applied to the flat faces in which the axons were cut longitudinally (or on the Y-Z plane with the included coordinate system), and the displacement boundary conditions were applied to the two remote points. The first remote point was fixed in all degrees of freedom, while the opposite remote point was stretched to a strain of 20% in the +Z direction. The applied boundary conditions can be found in Figure 20(A-C). The strain rate applied to the system is applied at a rate of 1.136 μm/sec.

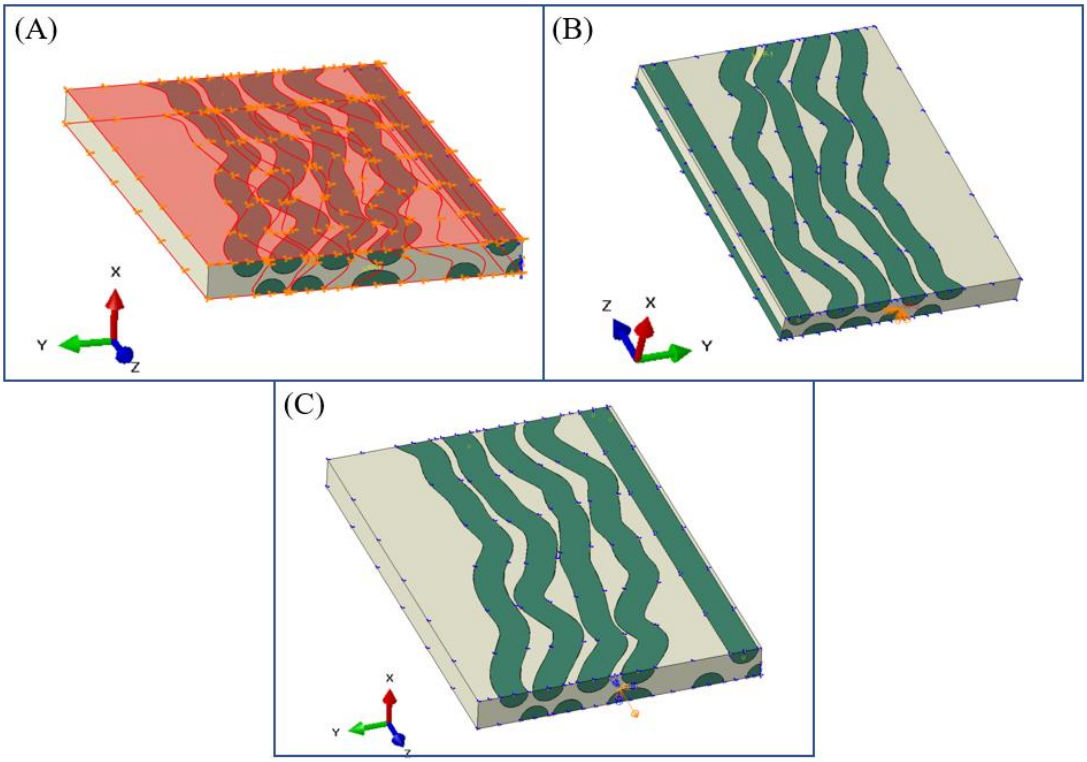

Figure 17: (A) X-symmetry applied to the top and bottom faces of the finite Element Model. (B) 20% strain applied to the remote point in the +Z direction. (C) All degrees of freedom fixed at the remote point opposite to the strain application.

Once the boundary conditions were applied, the finite element model was ready to be solved. The model was solved using a general static load step with the Abaqus implicit solver. Nonlinear geometry was used to accommodate the large displacements applied to the model and assigned hyperelastic material properties.

4.2 Sub-Model 2: Multiple Oligodendrocytes

Condition 2 added components representative of oligodendrocytes to the FE model. **Figure 18** shows an oligodendrocyte in the cerebellum of a newborn human brain [21]. This image provided a guideline to creating an oligodendrocyte feature inside of the FE model. A single oligodendrocyte can wrap around multiple axons to provide insulation for the

electrical signals as well as create a supporting scaffold for the axons. Oligodendrocytes have been recorded to bond to up 80 separate axons. Including 80 axons is beyond the scope of current model, but Oligodendrocytes are still to be used to tie all 10 axons together. The goal of this model is to show proof of concept that oligodendrocytes can be represented in a finite element environment.

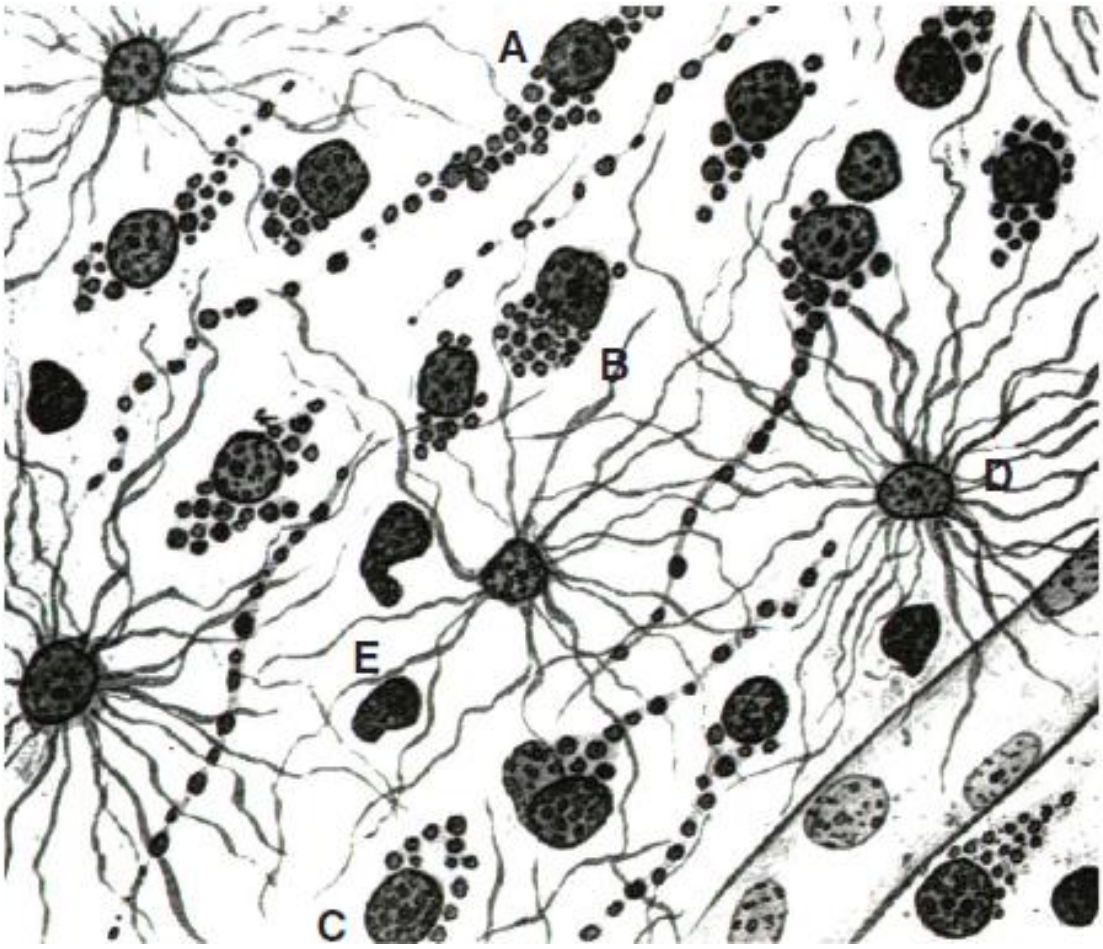

Figure 18: Image of multiple oligodendrocytes inside of a fetal human brainstem [21].

The same FE model from Condition 1 was used (including all load cases, boundary conditions, and constraints), but some changes were made to the model geometry to accommodate the addition of oligodendrocytes. First, oligodendrocyte locations were to be chosen. A plane in between the axons layers was added to the model for the placement of

the oligodendrocyte centers. 25 points were created, evenly spaced in a grid on the plane created in the previous step. The planar location and points for the oligodendrocytes is shown in Figure 19.

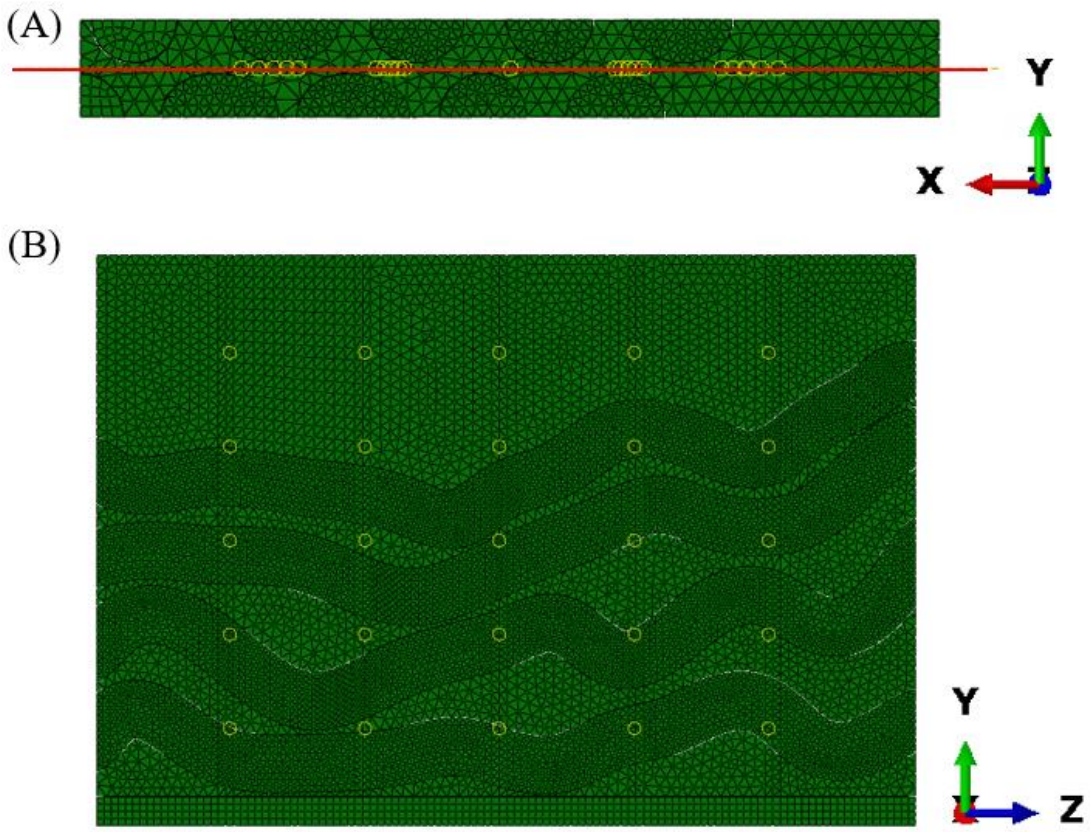

Figure 19: (A) Plane set between the axon layers. (B) points on the above plane where oligodendrocyte centers will be placed.

The oligodendrocyte center was generated as a sphere with a radius of 0.025 µm. The sphere was designed to sit in between the axon layers, but also so it will not overlap with the surrounding axons. **Figure 20** shows the geometry used to represent the center of the oligodendrocyte and the mesh generated. The material properties for the Generalized Ogden model of hyperelasticity that were assigned to the Oligodendrocyte were found from

Shreiber's research [17]: μ_o = 32.8 kPa, α = 8.22. This material was modeled as incompressible.

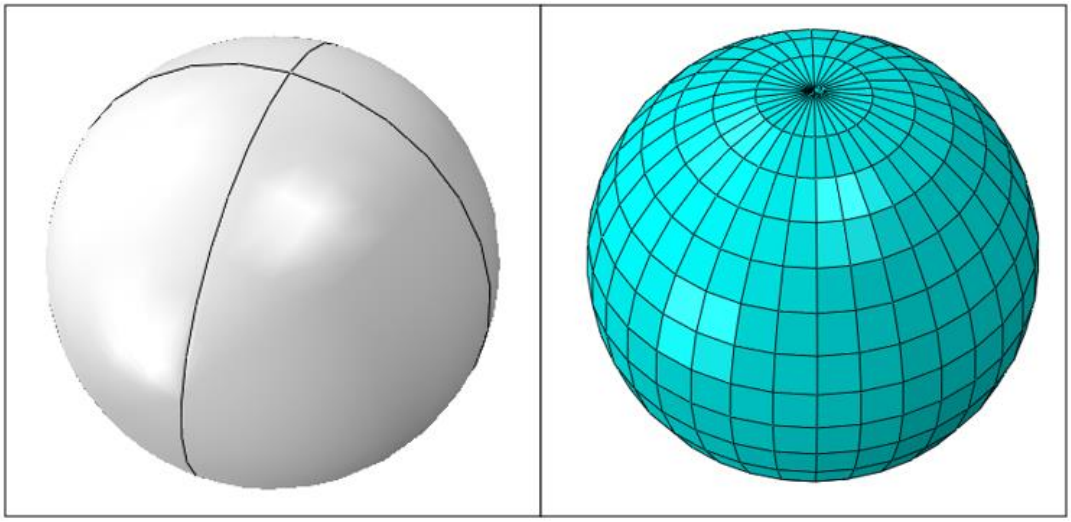

Figure 20: 3D generated model of the oligodendrocyte center and the resulting mesh.

25 of the oligodendrocyte center spheres were implemented into the model with the center points of each sphere scoped to one of the points shown in **Figure 19.B**. The Abaqus Merge/Cut Instances tool was used to remove the redundant geometry between the axons and ECM. The meshed sphere instances were embedded into the ECM using a tie constraint between the outer diameter of the sphere and the inner diameter of the region where the sphere geometry was removed from the ECM. A remote point was placed at the center point of each sphere, where a continuum coupling constraint was used to tie the nodes on the outer diameter of the oligodendrocyte to the center point. The continuum coupling constraint allows for the nodes on the outer diameter to interact with the surrounding ECM.

The next step in adding the Oligodendrocytes to the model required adding a condition where the oligodendrocyte was able to wrap around the outer diameter of the

axon. All ten axon instances in the FE model were sliced in an equally spaced pattern of datum planes to allow for five oligodendrocyte bonds per axon. See

Figure 21 for a detailed view of the plane distribution and sections of axons cut. Each narrow axon section that was cut was used for an oligodendrocyte bond.

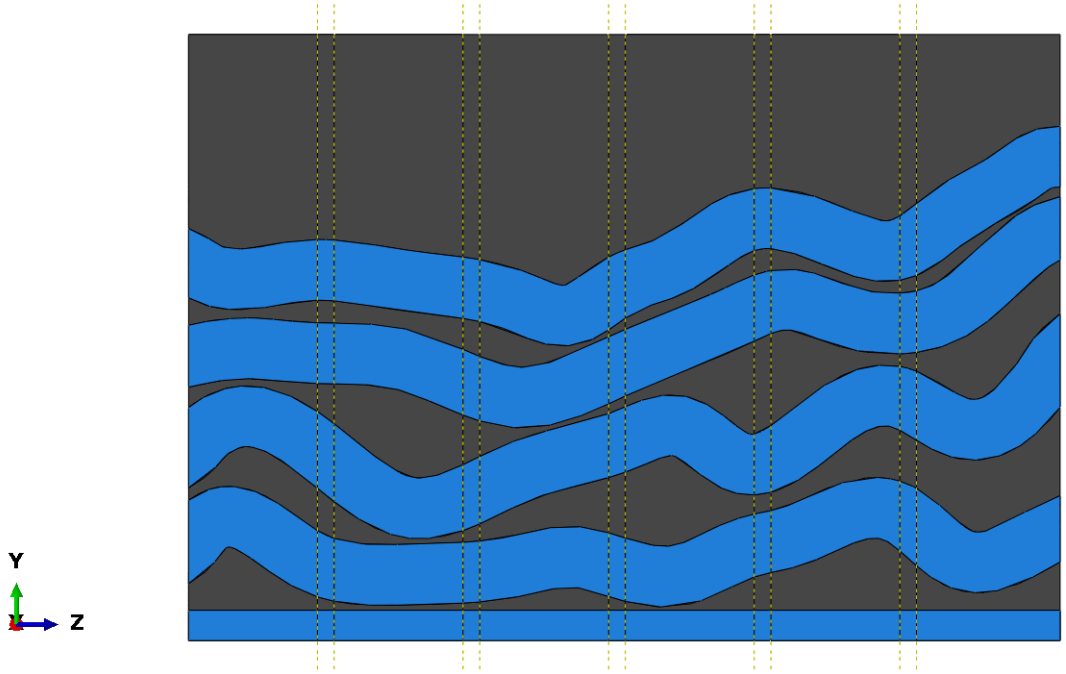

Figure 21: Sliced regions used to split axons for oligodendrocyte bonding.

The narrowly sliced regions of the axons are used to simulate the regions where the oligodendrocyte arms wrap around the outer diameter of the axon. A remote point was placed in the center of the axon diameter and tied to the nodes on the outer diameter of the axon mesh using a continuum coupling condition. A continuum coupling condition was used so that the axons would still be able to deform at the regions where the oligodendrocytes are bonded. A kinematic couple would have created stiff "rings" around the axons rather than allowed for interaction with the surrounding regions. **Figure 22** shows the regions where the continuum coupling constraints were applied.

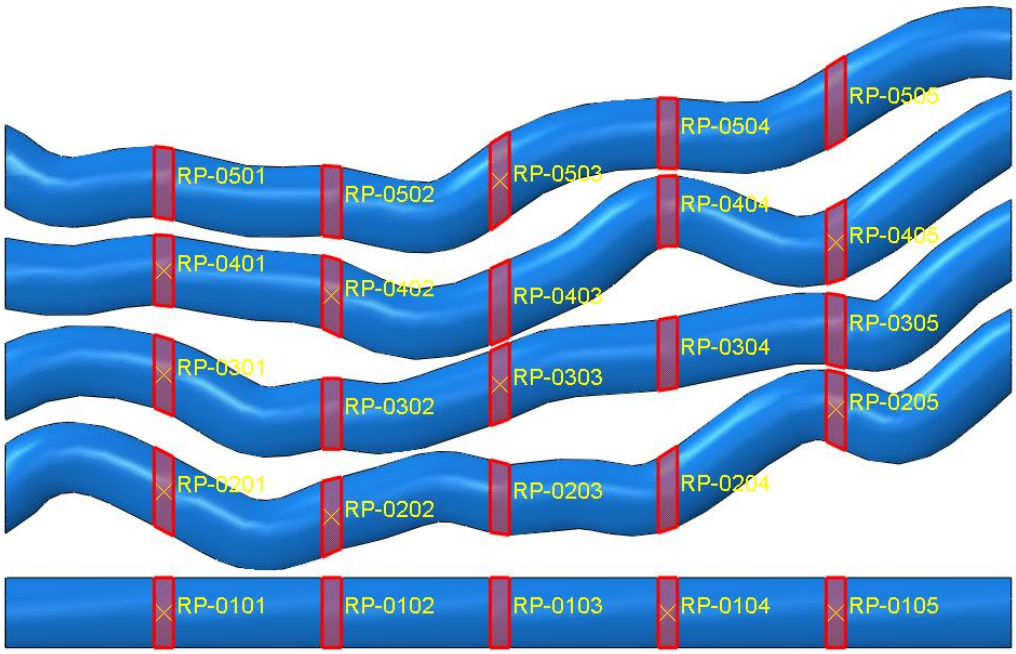

Figure 22: Regions on the axon outer diameter and the accompanying remote points tied with a continuum coupling condition.

Finally, the axons and the oligodendrocytes were tied together using a spring-dashpot connection. The spring-dashpot tool in Abaqus assigns a linear element representative of a spring and dashpot in parallel. The limitation of the spring-dashpot tool only allows for a single spring and dashpot to act in parallel, so a hyperelastic spring was unable to be created at this time.

In the current sub-model, the oligodendrocytes are acting in tension and compression as the finite element model is subjected to a uniaxial tension. Test data for a single oligodendrocyte in tension and compression was unable to be found, so arbitrary values of 10 N/m and 1 kg/s was used for the spring rate and damping coefficient, respectively. The values were selected so that the FE model would still be affected by the addition of the oligodendrocytes, but it would not drastically change the properties of the axons/ECM as the system is subjected to external loading.

The distribution of axon-oligodendrocyte connections was generated by manually observing the model and attaching all axon remote points that were within two axon diameters to the nearest oligodendrocyte. The maximum number of axons connected to a single oligodendrocyte was 5, with some oligodendrocytes only connecting to one axon. The selection of oligodendrocyte-axon connections was not limited to a single plane – the oligodendrocytes were connected to any axons that fit the proximity requirement. The Oligodendrocyte-Axon link in **Figure 23** shows the distribution of oligodendrocyte to axon connections. Each spring-dashpot connection is represented by a pink line. The model was subjected to identical boundary and load conditions as specified in **Section 3.1.**

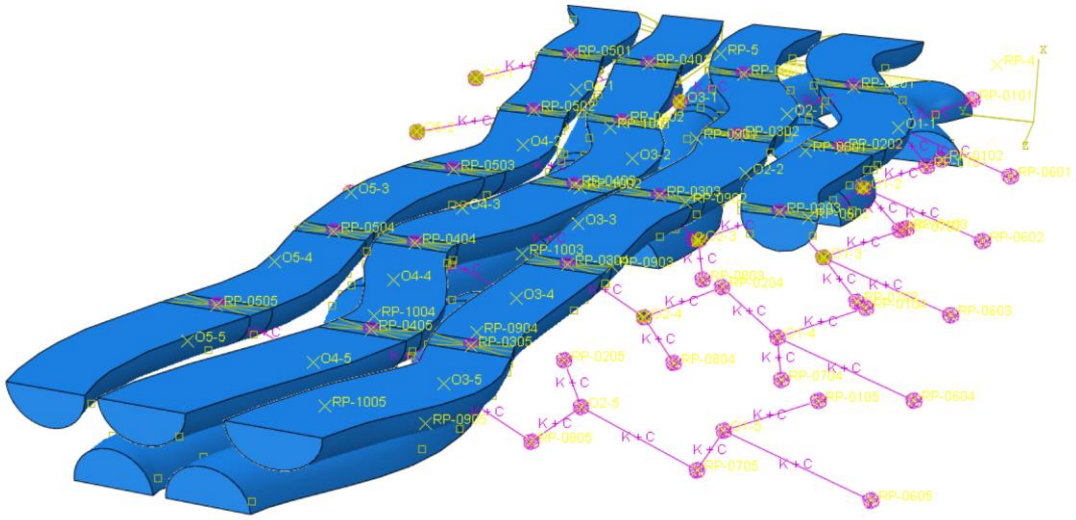

Figure 23: Oligodendrocyte connections represented by spring-dashpot connections. Components of the assembly have been removed for clarity.

4.3 Sub-Model 3: Single Oligodendrocyte

To supplement Condition 2, a third sub-model was created with a single oligodendrocyte tied to multiple axons. Oligodendrocytes are recorded to tie up to 80

axons, so a proof of concept analysis was to be run with all 10 axons in the FE model tied to a single oligodendrocyte. An oligodendrocyte was placed in the center of the ECM model using the same geometry as detailed in **Figure 20** and embedded in the ECM using the same technique as detailed in **Section 4.2 .**

The oligodendrocyte is tied to the center and both ends of all 10 axons for a total of 15 connections. A remote point at the center of the oligodendrocyte is scoped to the outer diameter of the oligodendrocyte sphere using a continuum coupling condition. At the center and end points on each axon, a remote point is scoped to the center of the axon and tied to the outer diameter using a continuum coupling condition as well. **Figure 24** shows the faces and remote points used to tie the axons to the oligodendrocyte.

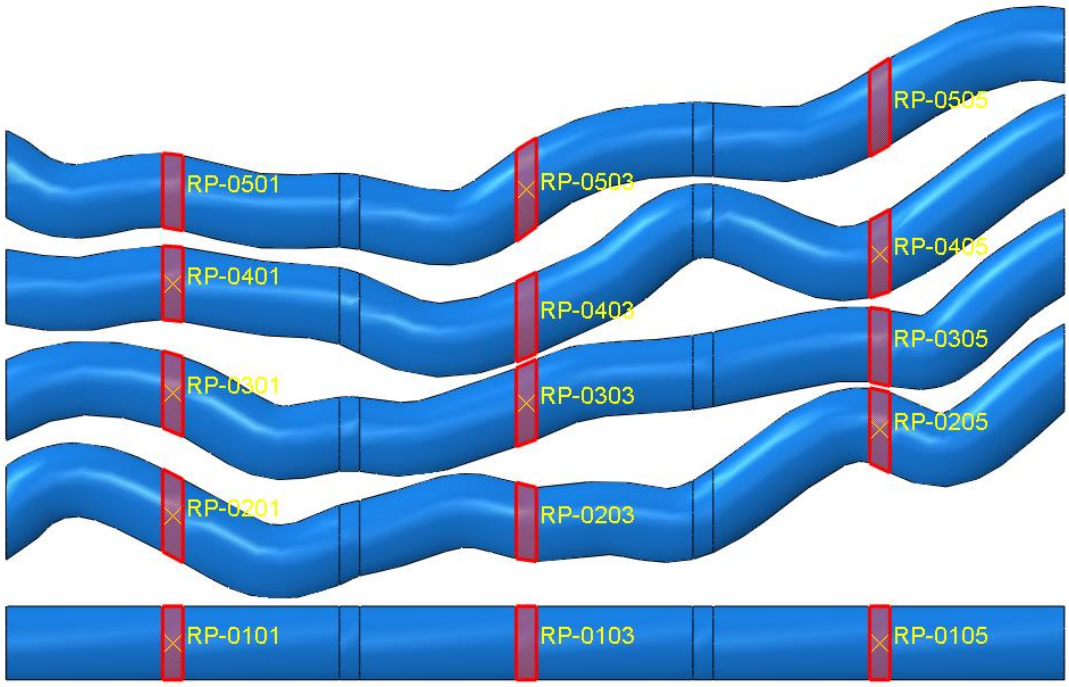

Figure 24: Axon faces and accompanying remote points used to tie axons to the oligodendrocyte.

As used previously, a spring-dashpot connection was used to tie the oligodendrocyte to the axons. The spring and dashpot are connected in parallel, using a spring rate of 10 N/m and a damping coefficient of 1 kg/s^2. **Figure 25** shows the oligodendrocyte-axon connections made inside of the FE model. The model was subjected to identical boundary and load conditions as detailed in **Section 3.1.**

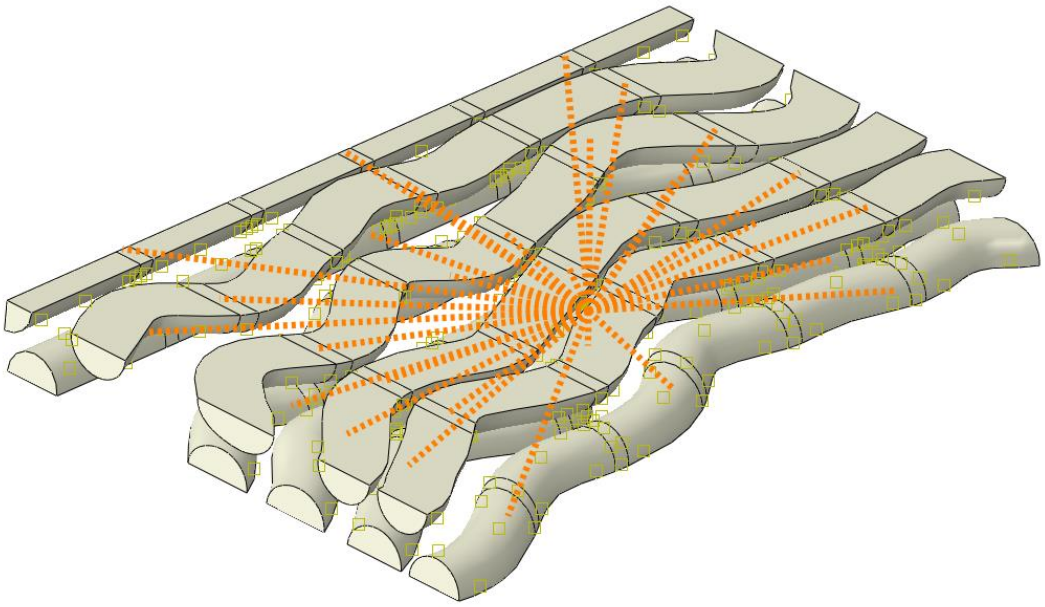

Figure 25: Axon-oligodendrocyte connections for the third FE submodel.

5.0 Chapter 5: Results

All results were found using the Abaqus static implicit solver. Results are presented in figure form at the beginning of **Section 5.1** and **Section 5.2** , with a discussion of the results following the presented figures. It is to be noted that that the stress results calculated shall be divided by a factor of 10^6 to compensate for modeling in micro-meters. The mesh lines have been removed from the general views in the visualization model to clearly view the stress contours.

5.1 Condition 1 Results and Discussion

The results from for the first sub-model are detailed in the following section. All contour plots have been limited to 300 Pa for clarity. The global coordinate system has been included with each system-level figure for clarity and is referenced to give the readier information on the model orientation. **Figure 26** shows an isometric view of the von Mises results from the condition 1. The quarter axon at the bottom left of **Figure 26** does not interact with the ECM due to a lack of ECM material surrounding the bottom edge of the finite element model. This instance acts solely in tension.

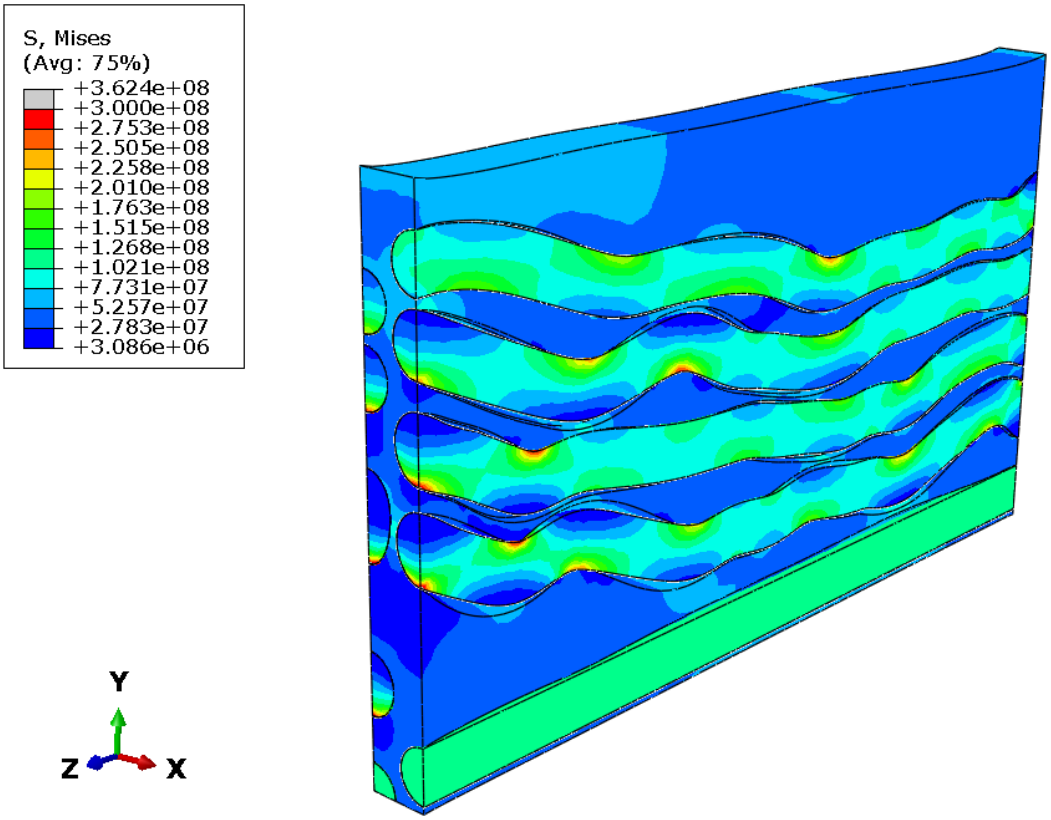

Figure 26: Condition 1 results, isometric view

Figure 27 shows the von Mises stress results in the finite element model. The model is oriented with the x-axis pointed out of the page.

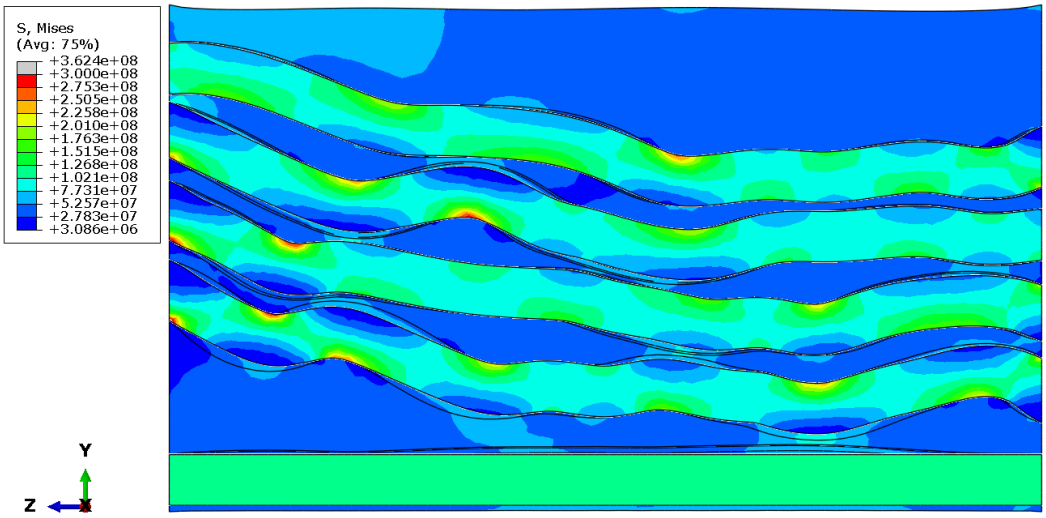

Figure 27: Condition 1 results, positive x-axis pointed out of page.

Figure 28 shows the von Mises stress results in the finite element model. The model is oriented with the x-axis pointing into the page.

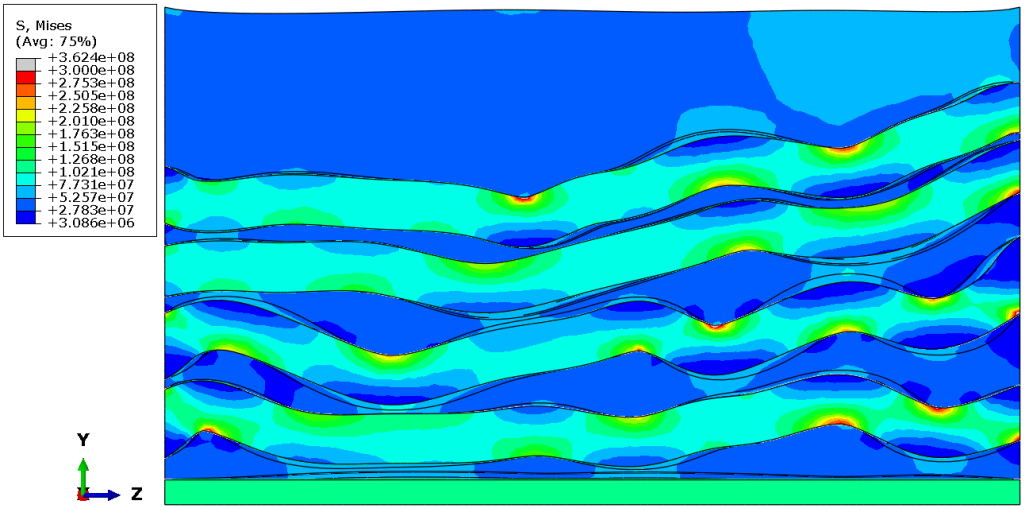

Figure 28: Condition 1 results, positive x-axis pointed into page.

Figure 29 shows the von Mises stress results in the finite element model. The model is oriented with the z-axis pointing out of the page. High stress regions at the bottom of the axons generated from the applied boundary condition. The kinematic coupling condition fixes all nodes on the face in space while the surrounding nodes are free to react to the applied force.

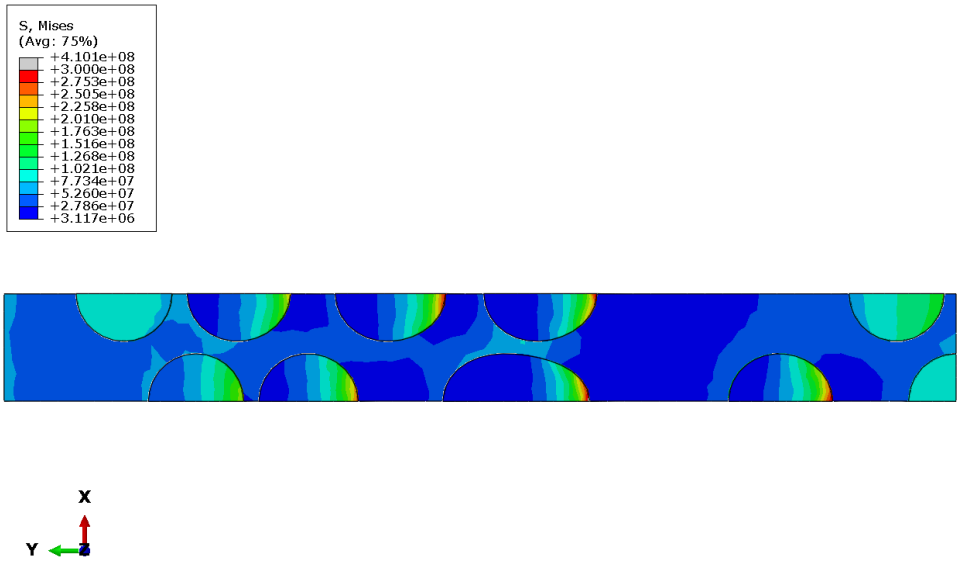

Figure 29: Condition 1 results, positive z-axis pointing out of page.

Figure 30 shows the Von Mises stress results in the finite element model – the model is oriented with the z-axis pointing into the page. Again, note the stress contours where the undulated axons and ECM contact.

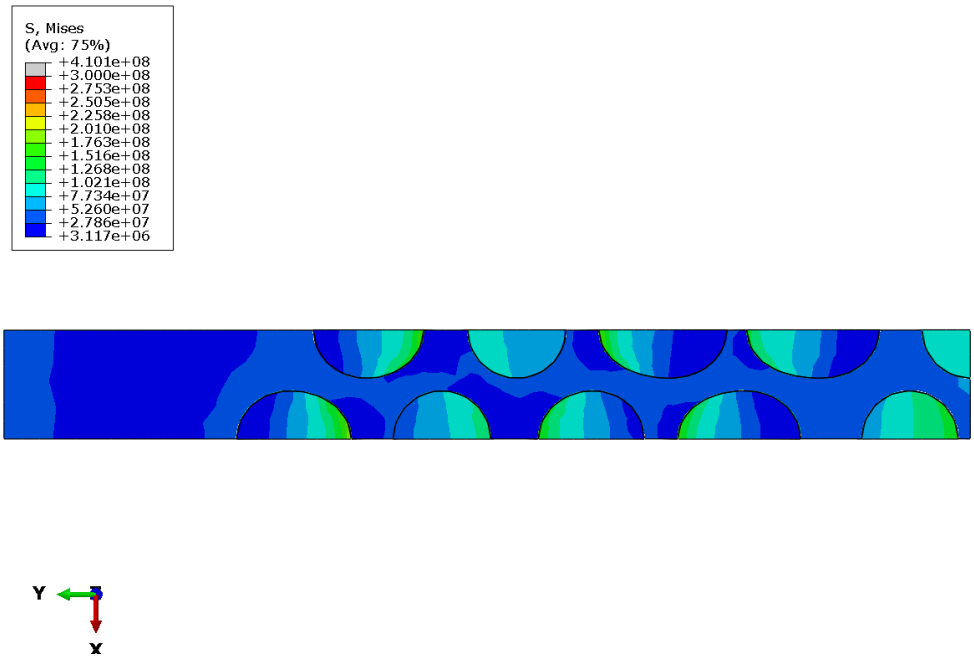

Figure 30: Condition 1 results, positive z-axis pointing into page.

Figure 31 shows the von Mises stress results in the cylindrical faces of the axons. The model is oriented with the z-axis pointing out of the page.

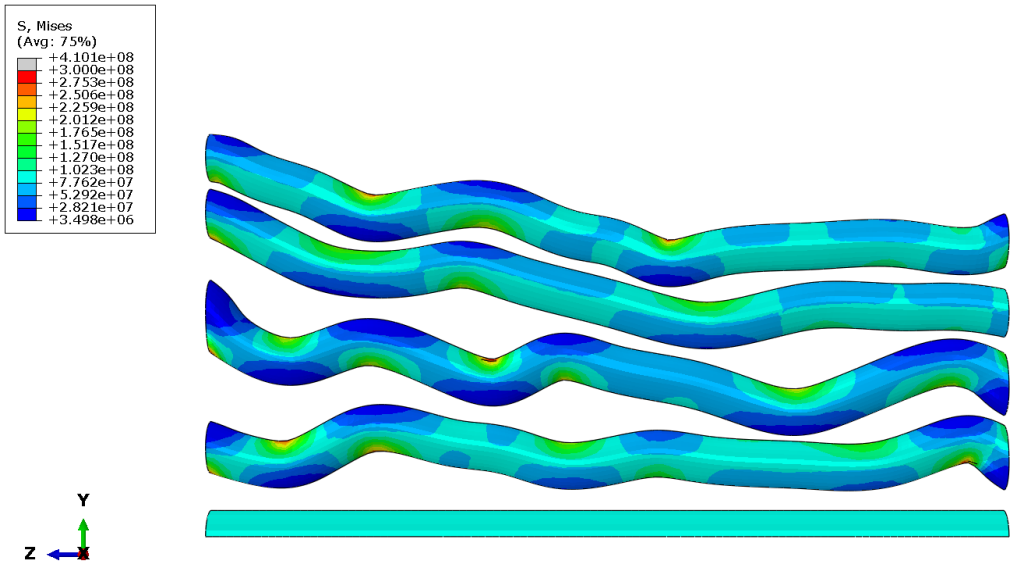

Figure 31: Stresses in the cylindrical faces of the axons, positive x-axis pointing out of the page.

High stresses occur in the concave regions of the undulated axons. Bending stresses can be seen at the inflection points in the axon paths (to be discussed later). **Figure 32** gives a magnified view of the bending stresses observed.

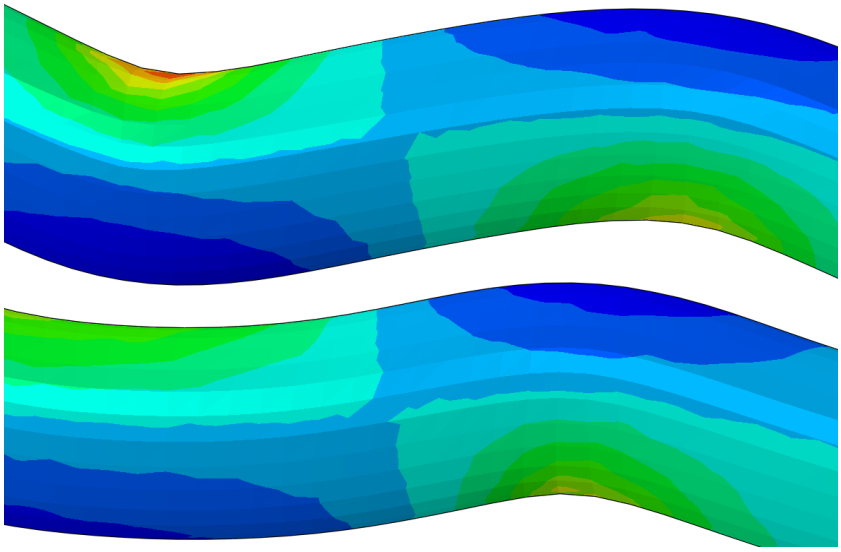

Figure 32: Regions where bending stresses are shown. The regions where the stress reverses abruptly from compressive to tensile stress indicates a bending stress.

Figure 33 shows the von Mises stress results in the cylindrical faces of the axons. The model is oriented with the z-axis pointing into the page. The axons shown this region (primarily the second from the bottom) showed multiple instances where bending stress occurred over a short axon length. Bending stresses occurred at inflection points in the paths that the axons followed. **Figure 34** details a region with multiple bending stresses.

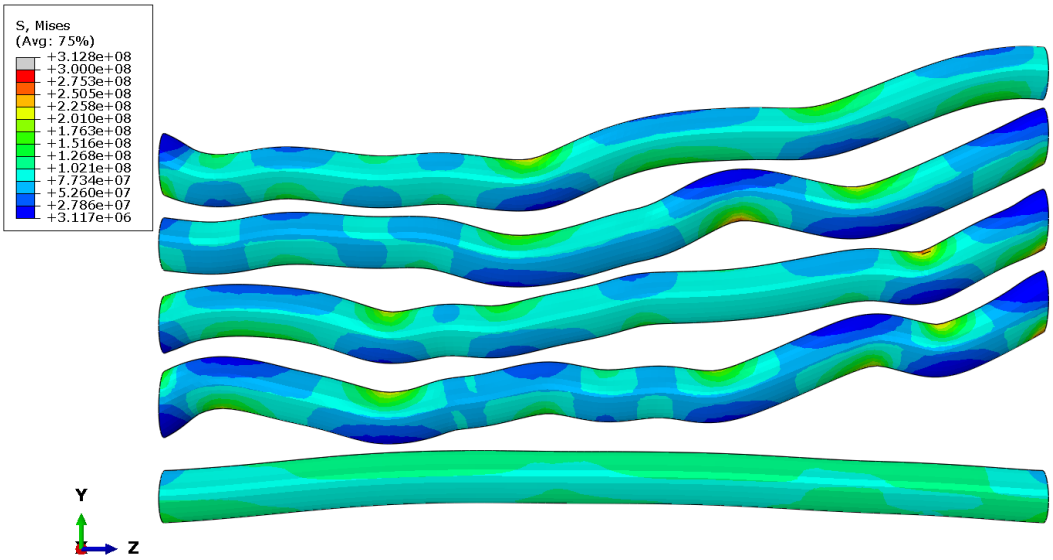

Figure 33: Stresses seen in the cylindrical faces of the axons, positive x-axis pointed into the page.

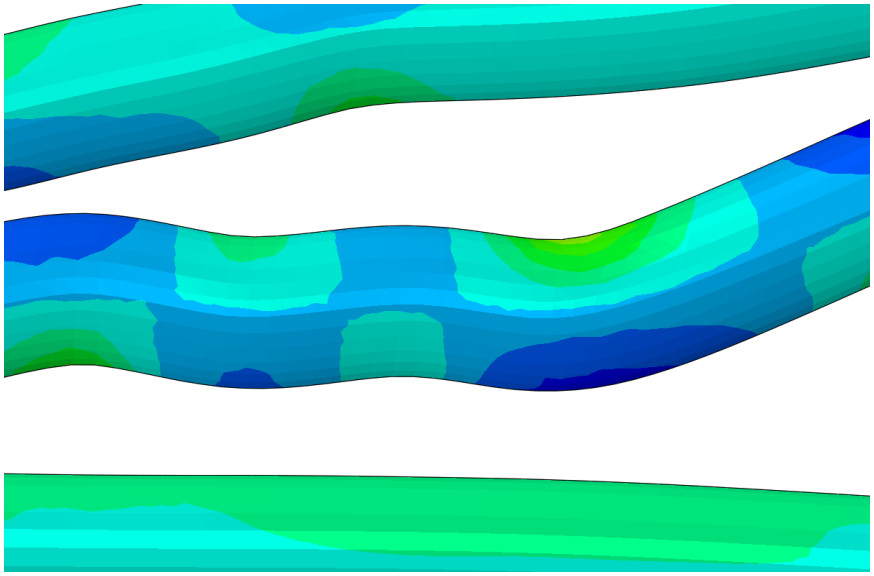

Figure 34: Magnified view of a region where multiple bending stresses occur in a short distance.

Figure 35 and **Figure 36** show the von Mises stress measured in the ECM under uniaxial tension. These measured stresses are for reference only, as the mesh in the ECM was not refined enough to calculate accurate contact stresses.

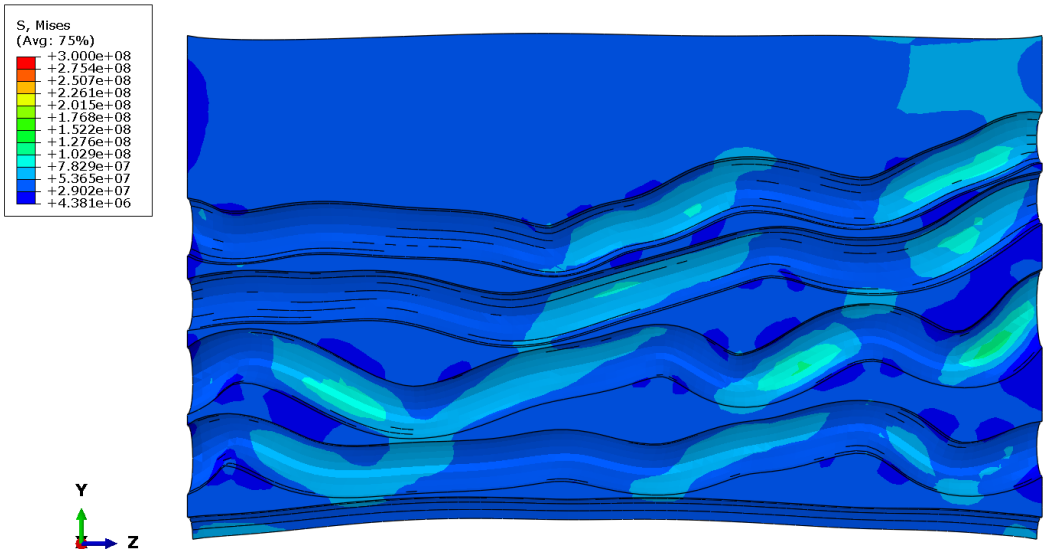

Figure 35: Reference view of stresses calculated in the ECM, positive x-axis pointed into the page.

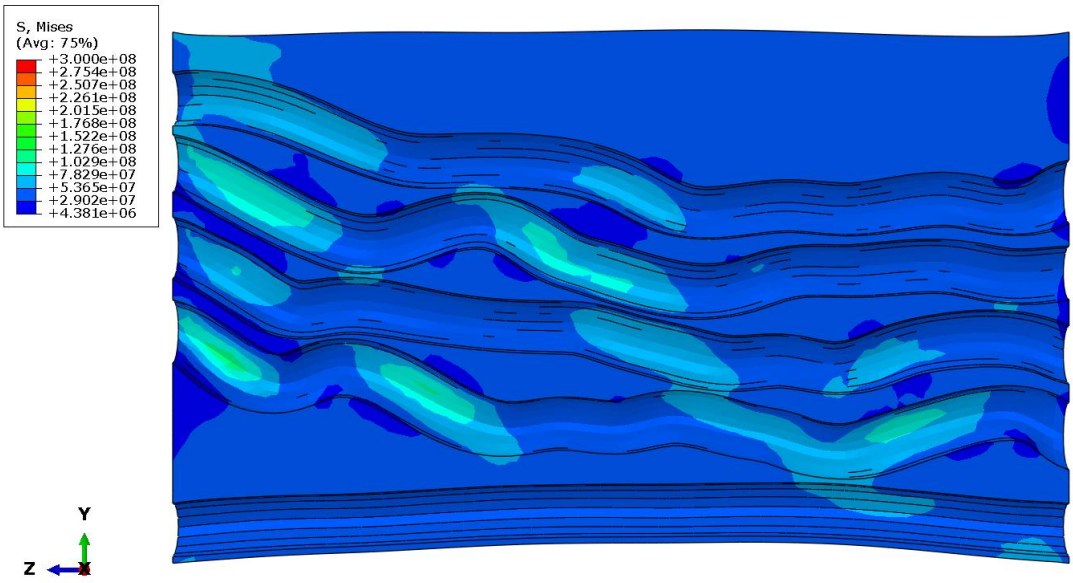

Figure 36: Reference view of stresses calculated in the ECM, positive x-axis pointed out of the page.

The maximum stress recorded in the first submodel was 410 Pa. The high stress regions occurred at a single element directly near a boundary condition where all degrees of

freedom were fixed. The von Mises stress measured in this region is can be ignored, as a fully fixed condition is not representative of the real system. **Figure 37** shows the singular node and the surrounding region. The high stress regions in the axons occurred at the inner radius of all tight bends where stress concentrations are expected to occur. Besides the singular node, the maximum stress recorded in the finite element model was 320 Pa. See **Figure 38** for more information.

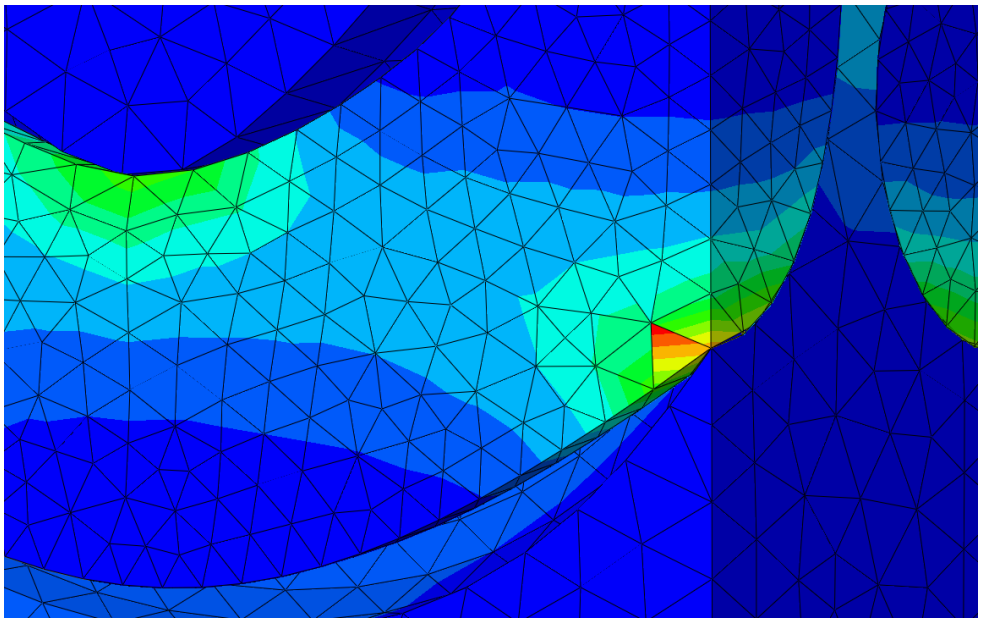

Figure 37: Singular node found in the finite element model. This occurs from to the proximity to the applied boundary condition.

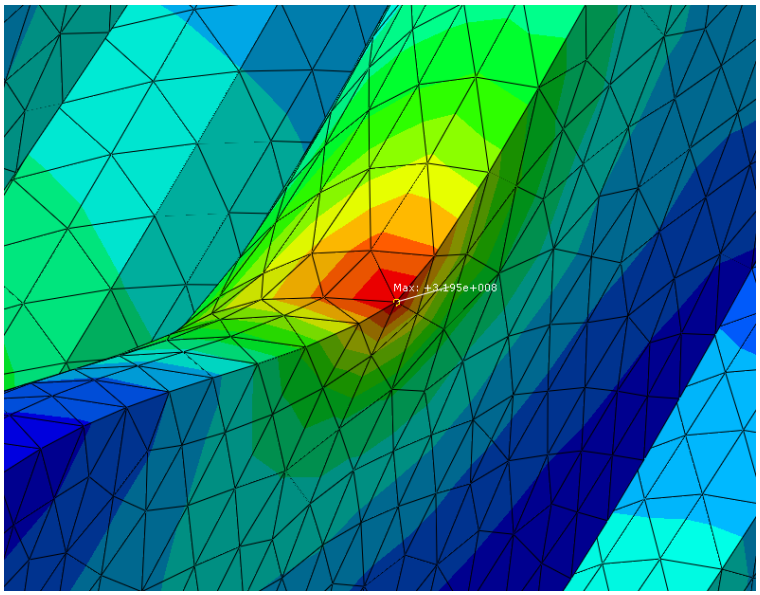

Figure 38:Maximum stress recorded in the finite element model for condition 1

The bending stresses found in **Figure 32, Figure 33,** and **Figure 34** are an unexpected result of the analysis. Previous research indicates that tensile failure is the proximal cause of TBI. In Bain's work, it was postulated that as the axons are subject to a uniaxial tension, the undulation decreases until a point where the axon is acting fully in tension. This remains true and is supported by the analysis results, but the bending stresses introduce another potential failure mode: fatigue.

The bending stresses seen at each inflection point indicate that full stress reversal can occur if the region is subjected to repeated tensile and/or compressive stresses. Bending stresses were also recorded multiple times on a single axon instance – increasing the probability of fatigue damage. The magnitude of the stresses seen in the axons will dictate whether they fail under low or high cycle fatigue. A fatigue analysis where the axons are subjected to both compression and tension under a prescribed number of cycles will be a sufficient complimentary analysis, but it is outside the scope of this current effort.

As the axons were subjected to the uniaxial tension, the disparity in material properties cause the ECM and the axon models to deform at different rates. The result of the tensile load caused that axons and ECM to separate in multiple regions – as expected in the non-affine condition. The result is detailed in **Figure 39.**

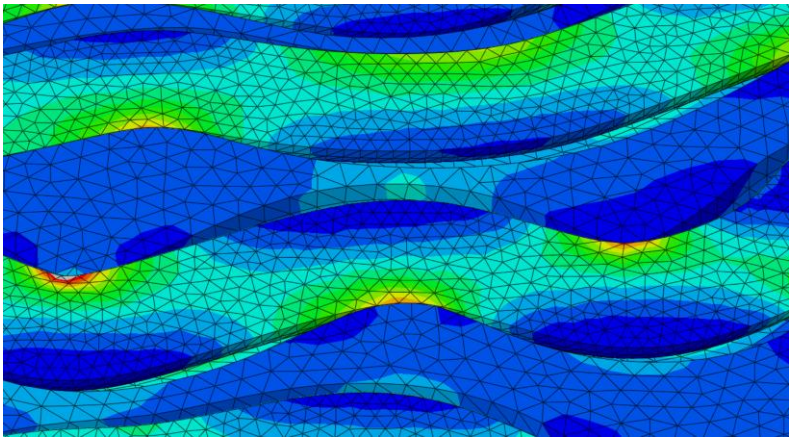

Figure 39: Separation between the axons and ECM resulting from the uniaxial tension applied.

5.2 Condition 2 Results and Discussion

The results from the finite element model for condition 2 are detailed in the following section. All contour plots have been limited to 300 Pa for clarity. The global coordinate system is for clarity and is referenced to give the readier information on the model orientation. Spring elements have been left in the figures for the reader to visualize where the connections occur. **Figure 40** shows an isometric view of the von Mises stress results from load condition 2.

Note: The quarter axon geometry does not interact with the ECM due to a lack of ECM material surrounding the bottom edge of the finite element model. This instance acts solely in tension.

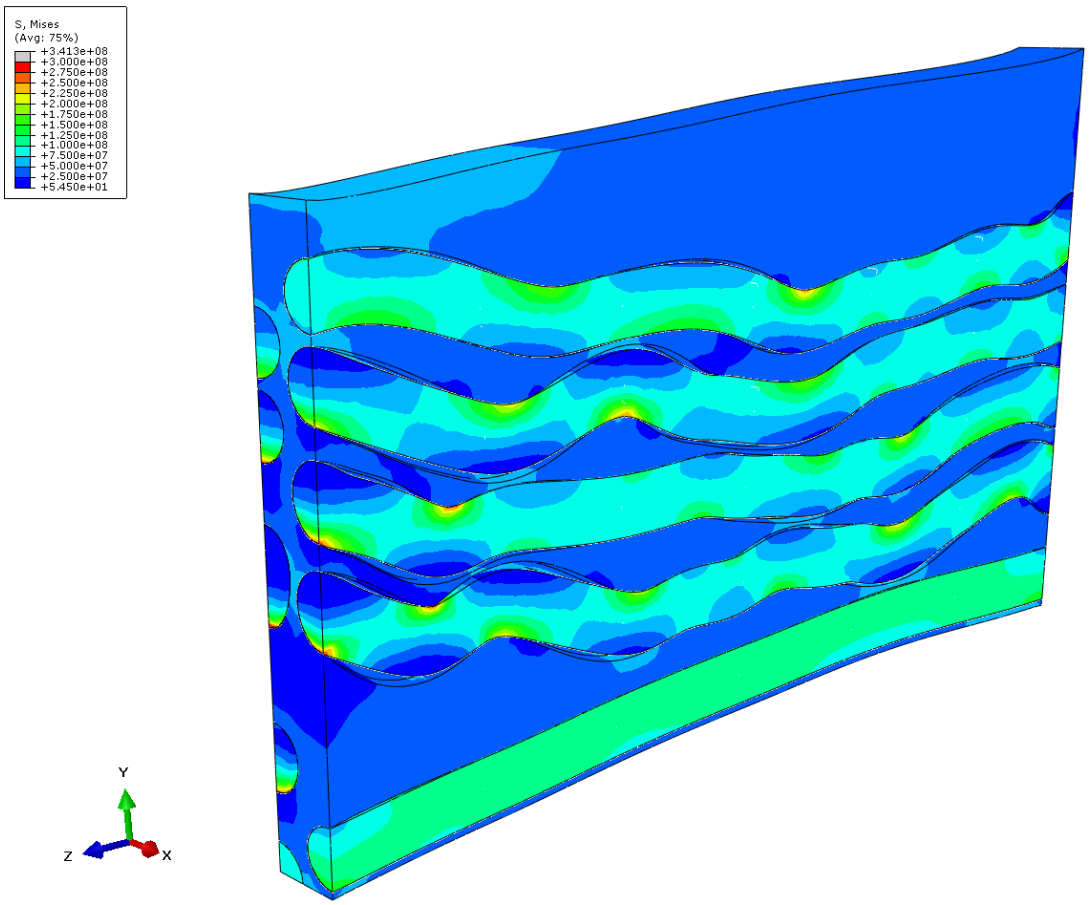

Figure 40: Isometric view of condition 2 results.

Figure 41 shows the von Mises stress results in the finite element model oriented with the global x-axis pointed out of the page.

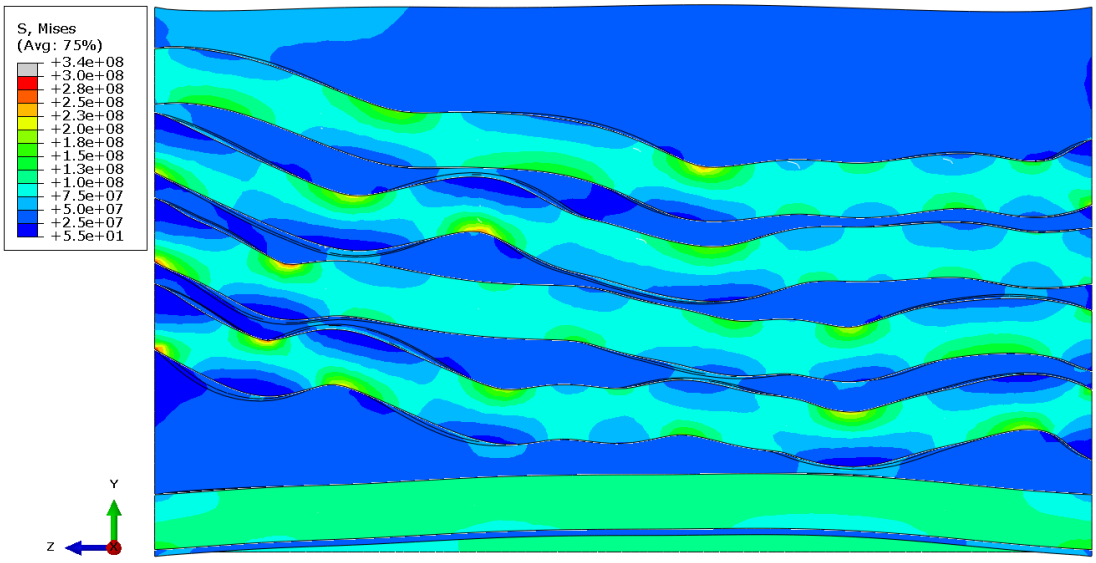

Figure 41: Condition 2 stress results, positive x-axis pointed out of page.

Figure 42 shows the von Mises stress results in the finite element model oriented with the global x-axis pointed out of the page.

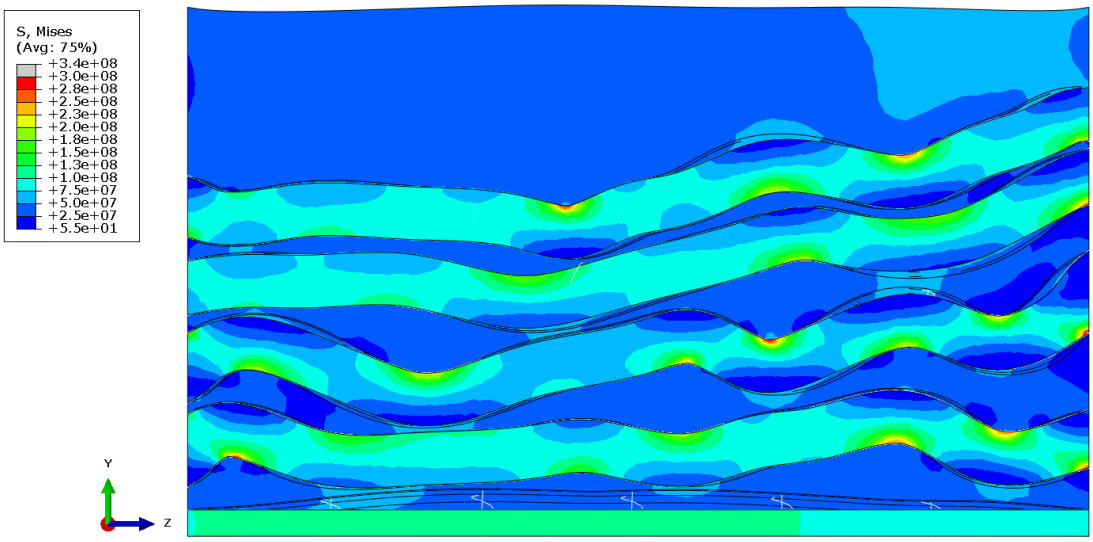

Figure 42: Condition 2 stress results, positive x-axis pointed into page.

Figure 43 shows the Von Mises stress results in the finite element model oriented with the global z-axis pointed out of the page. The high point stresses occur due to the zero-displacement boundary condition applied to the axon faces.

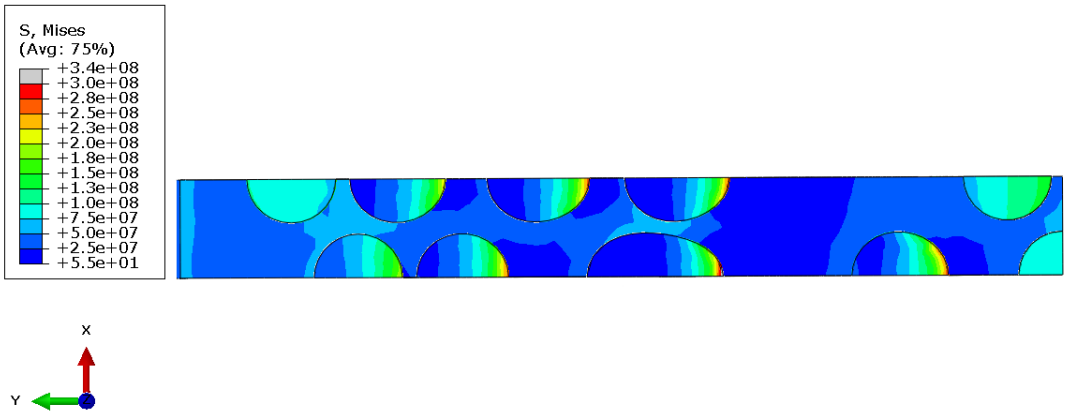

Figure 43: Condition 2 stress results, positive z-axis pointing out of page.

Figure 44 shows the Von Mises stress results in the finite element model oriented with the global z-axis pointed out of the page. As with the stress plot in the previous figure, the boundary condition application results in magnified peak stresses at the axon faces.

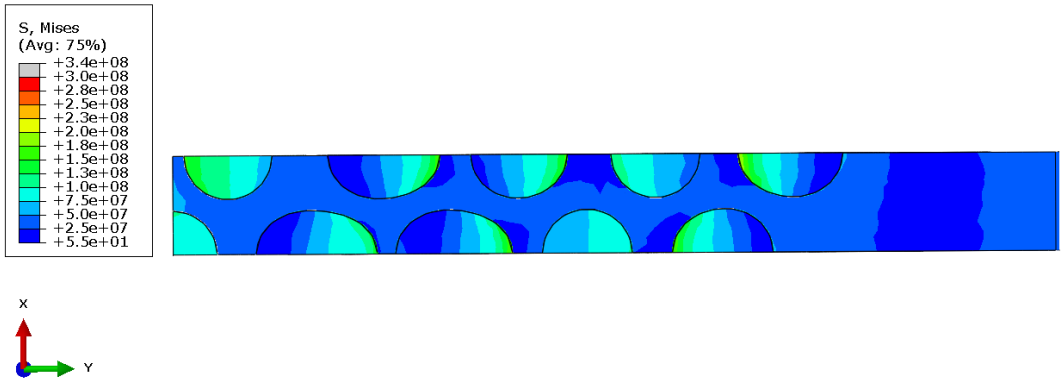

Figure 44: Condition 2 stress results, positive z-axis pointing into the page.

Figure 45 shows the von Mises stress results in the cylindrical faces on one of two rows of axons in the finite element model. The model is oriented with the x-axis pointed out of

the page. Note that the bending stresses still occur with the added support of the oligodendrocytes.

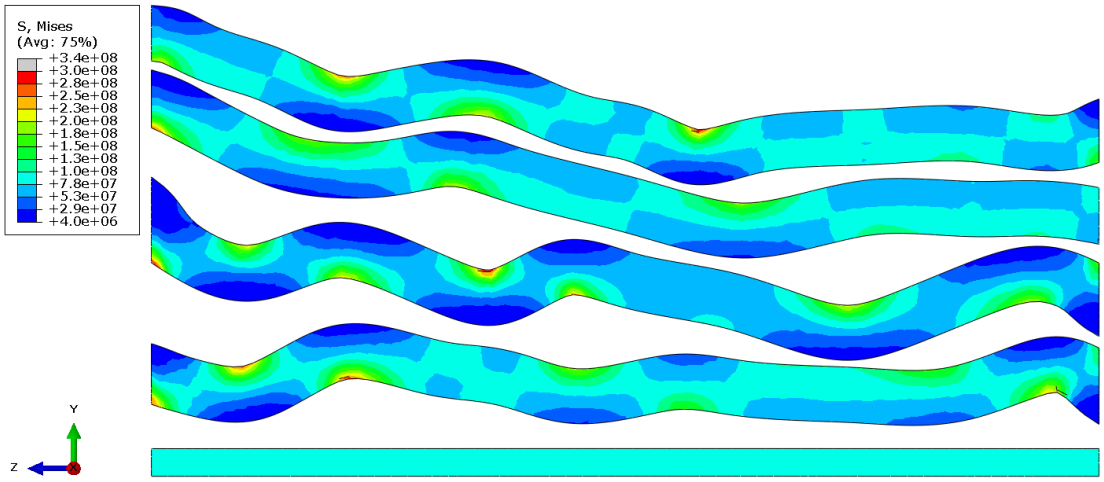

Figure 45: Stresses seen in the cylindrical faces of the Axons, positive x-axis pointed out of the page

Figure 46 gives a magnified view of the bending stresses recorded in the axons. In comparison to the stress results shown in **Figure 32**, the calculated stress fields in condition 2 show a more gradual transition from tensile to compressive stress.

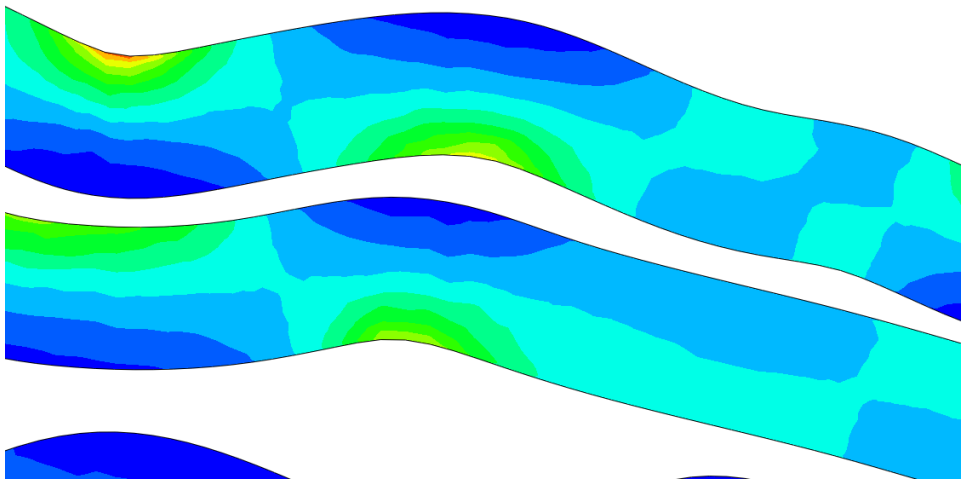

Figure 46: Magnified view of bending stresses in the Condition 2 stress results.

Figure 47 shows the stresses seen in the cylindrical faces in the second row of axons in the finite element model. As seen in the previous row of axons, it is to be noted that some bending stresses occur more gradually than sub-model 1. Compared to sub-model 1, the stresses seen are more evenly distributed across the axons.

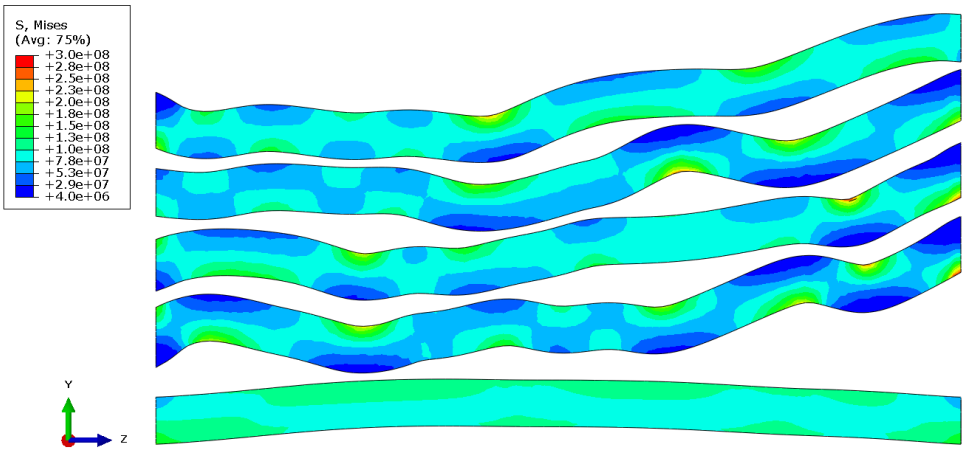

Figure 47: Stresses seen in the cylindrical faces of the axon, positive x-axis pointed into the page.

Figure 48 provides a magnified view of the more gradual bending stress patterns seen in the von Mises stress plots in the second row of axons.

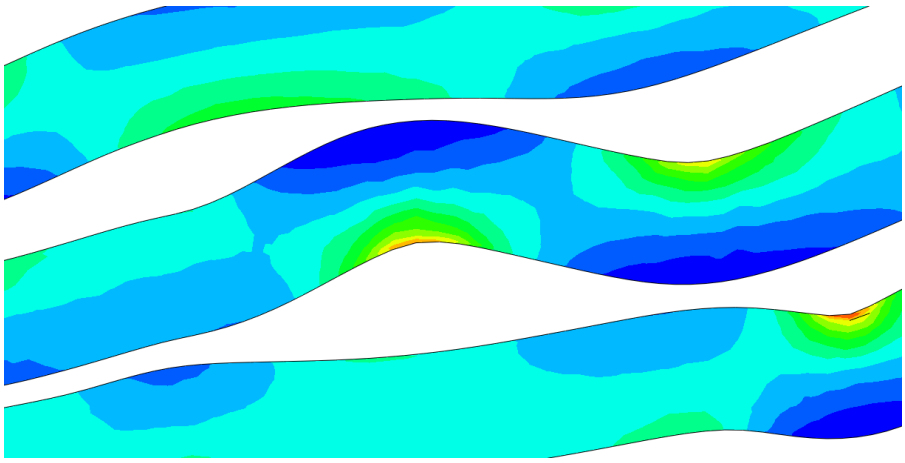

Figure 48: Magnified view of the gradual bending stress patterns seen in the second row of axons.

As provided with the stress results for the ECM in sub-model 1, the stress contours for the ECM are provided as **Figure 49** and **Figure 50** for reference. The figures are to provide further understanding stress field propagation in the ECM, but they do not yield accurate stress values.

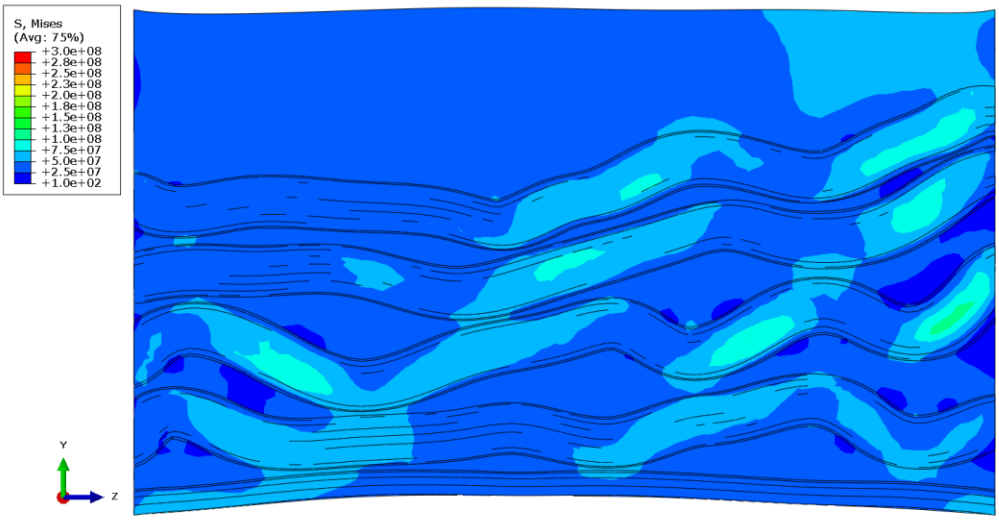

Figure 49: Stress fields in the ECM provided for reference. The model is oriented with the positive x-axis pointed into the page.

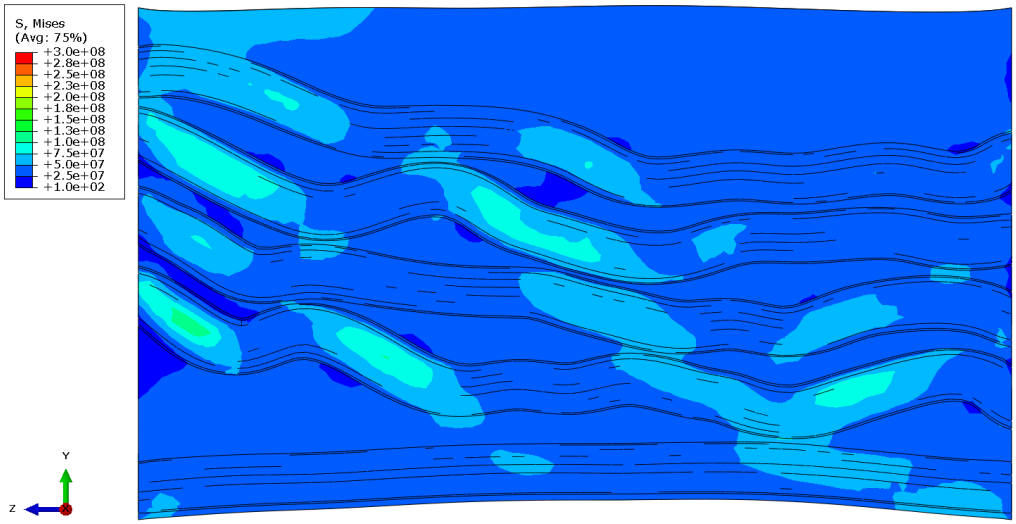

Figure 50: Stress fields in the ECM provided for reference. The model is oriented with the positive x-axis pointed out of the page.

As seen in the results from sub-mode 1, the applied fixed boundary condition caused a singular stress result due to the surrounding node's location and sharp corner that it is scoped to. This is a singular stress and does not represent an accurate stress seen in a real system. The node generated a stress of 340 Pa, as shown in **Figure 51**.

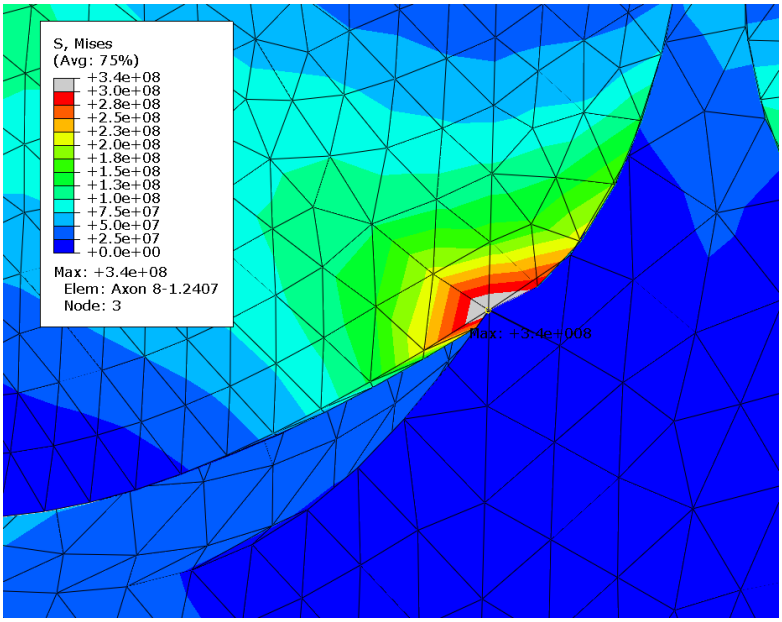

Figure 51: Singular node resulting from surrounding geometry and proximity to the applied boundary condition.

Outside of the singular node, the highest stress recorded in the axons was 310 Pa. This stress occurred at tight concave geometry and next to a region where the oligodendrocyte was tied to the axon. **Figure 52** details the region where the peak stress occurs and the surrounding geometry.

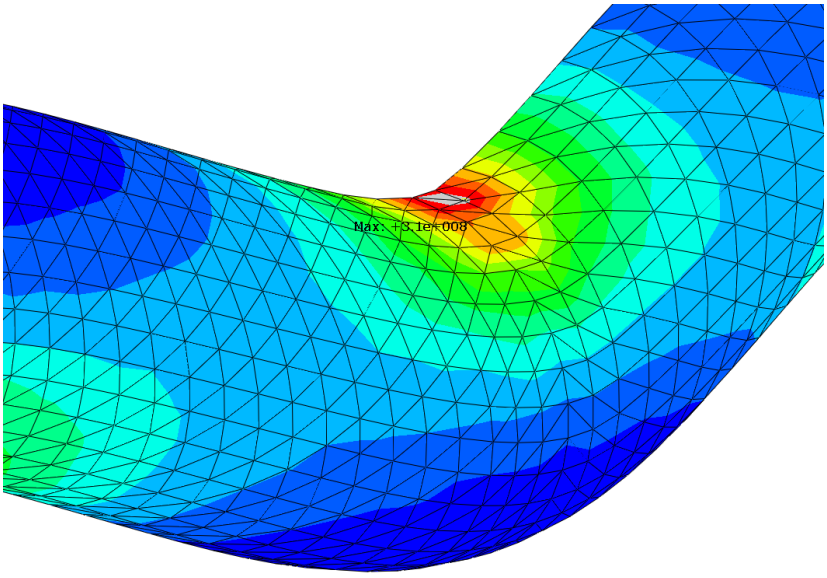

Figure 52: High stress region in an axon with high undulation and adjacent to an oligodendrocyte tie point.

As seen in condition 1, the tensile loading introduced gaps between the axon and the ECM. The gaps primarily occurred at regions of high tortuosity. The effect of the gaps forming is unknown. **Figure 53** shows an example of the gaps that formed between the Axons and ECM.

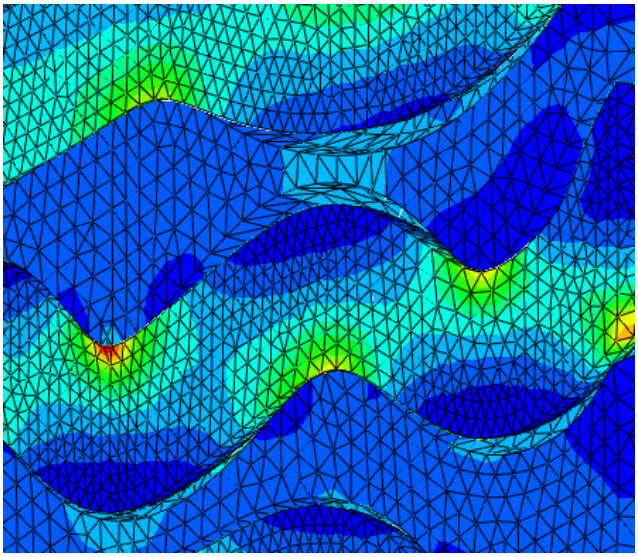

Figure 53: Gaps formed between the axons and ECM under tensile loading.

Bending stresses were also observed under loading in condition 2. A direct comparison to the other sub-models will be made at a later point in the report. The bending stresses seen were more gradual than in condition 1. Although the adjusted peak stress measured in the axons was 310 Pa, the general stresses recorded in the finite element model were more distributed between the regions tied with oligodendrocytes. For example, in **Figure 54**, the stresses are better distributed throughout the axons rather than multiple regions of alternating high and low stresses.

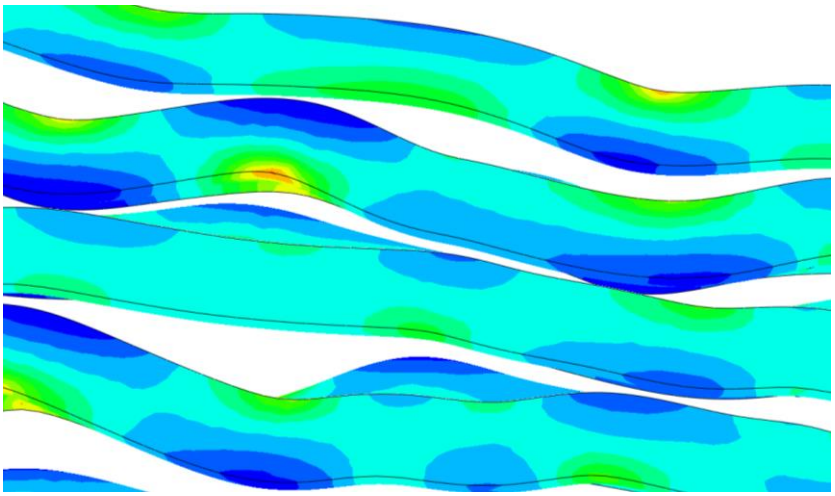

Figure 54: Magnified view of the stress distribution in a group of axons in sub-model 2.

5.3 Condition 3 Results and Discussion

The results for the third sub-model are detailed in the following section. All contour plots have been limited to 300 Pa for clarity. The global coordinate system has been included with each system-level figure for clarity and is referenced to give the readier information on the model orientation. **Figure 55** shows an isometric view of the von Mises results from condition 1.

Note: The quarter axon at the bottom left of **Figure 55** does not interact with the ECM due to a lack of ECM material surrounding the bottom edge of the finite element model. This instance acts solely in tension.

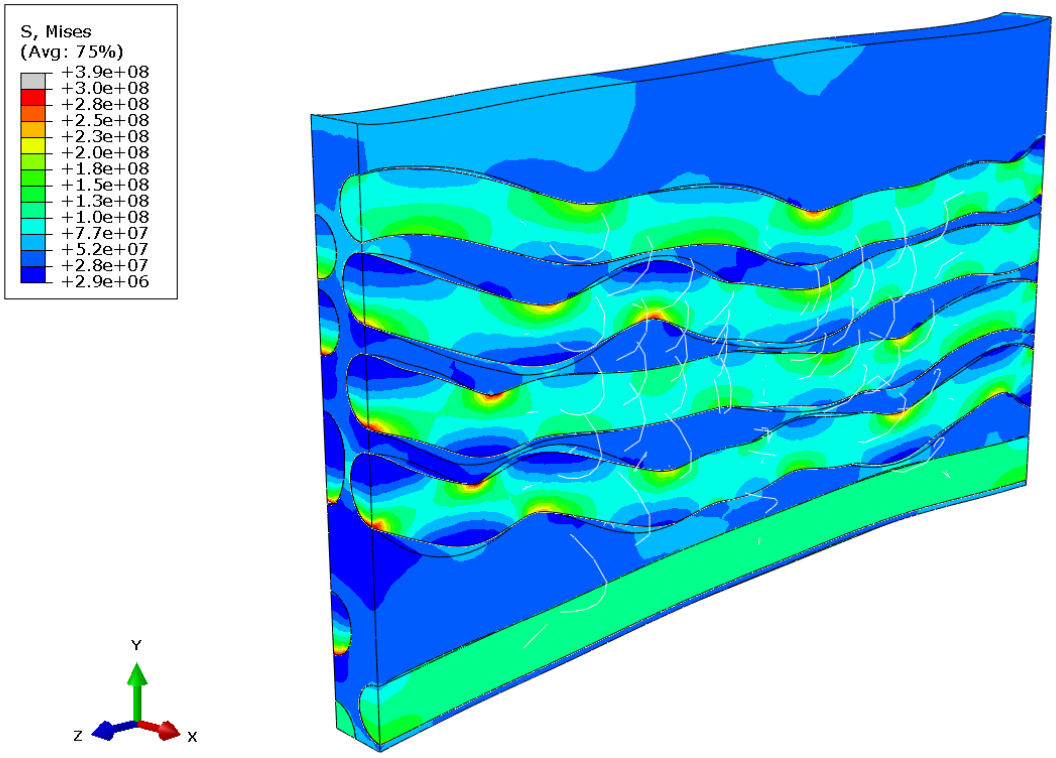

Figure 55: Isometric view of von Mises stress results in condition 3.

Figure 56 shows the von Mises stress results in the finite element model, oriented with the positive x-axis pointed out of the page.

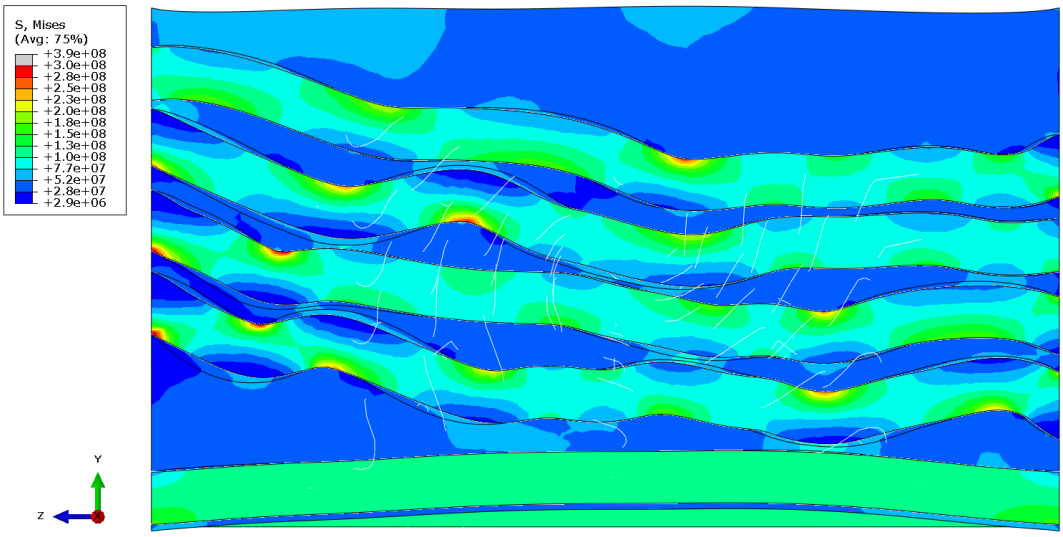

Figure 56: Condition 3 stress results, positive x-axis pointed out of page

Figure 57 shows the von Mises stress results in the FE model, oriented with the positive x-axis pointed into the page.

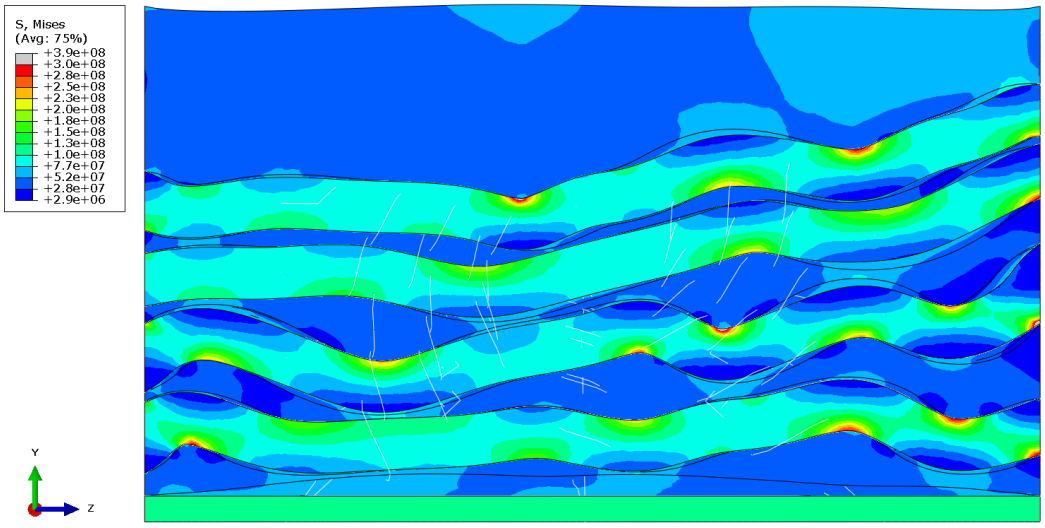

Figure 57: Condition 3 stress results, positive x-axis pointed into page.

Figure 58 shows the von Mises stress results in the FE model, oriented with the positive z-axis pointed into the page. The peak stresses on the axon faces occur due to the kinematic coupling along with the zero-displacement boundary condition applied to the axon faces.

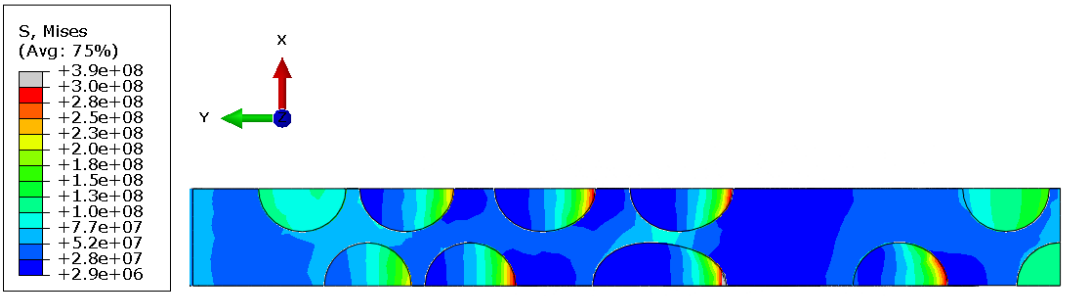

Figure 58: Condition 3 stress results, positive z-axis pointed out of page.

Figure 59 shows the von Mises stress results in the finite element model, oriented with the positive z-axis pointed into the page. The high stress regions at the edges of the axon faces occur due to the kinematic coupling condition fixing the nodes in all degrees of freedom.

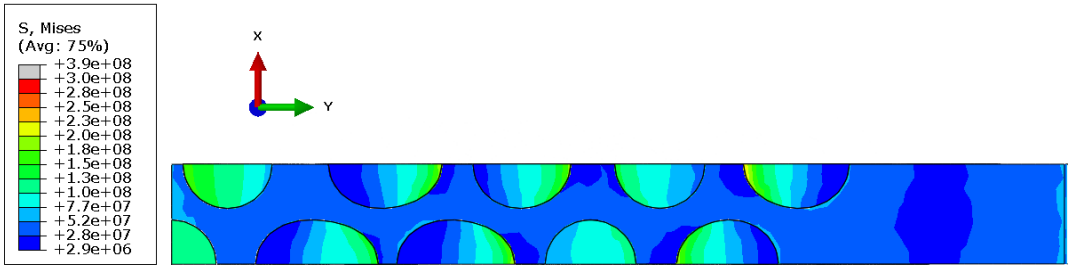

Figure 59: Condition 3 stress results, positive z-axis pointed into page.

Figure 60 shows the von Mises stress results on one of two axon rows, oriented with the positive x-axis pointed out of the page. The von Mises stresses shown are measured on the

cylindrical axon faces. Bending stresses are observed in the single oligodendrocyte condition.

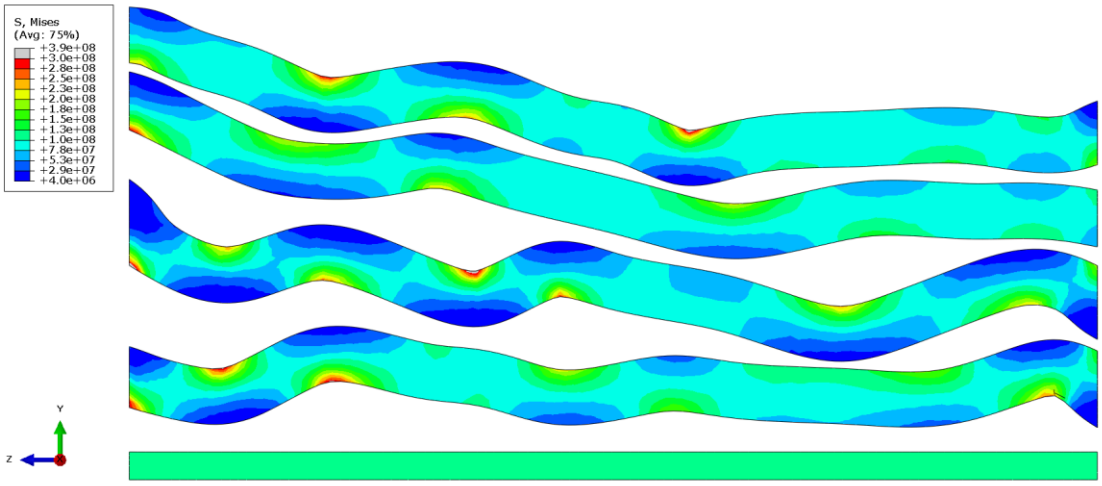

Figure 60: von Mises stresses seen in the cylindrical axon faces, positive x-axis pointed out of the page.

Figure 61 gives a magnified view of the stresses seen in the cylindrical axon faces. The concave regions of high axon undulation visibly have the highest stresses, with some reaching over 300 Pa. The bending stresses are seen between each inflection point in the undulated axon path.

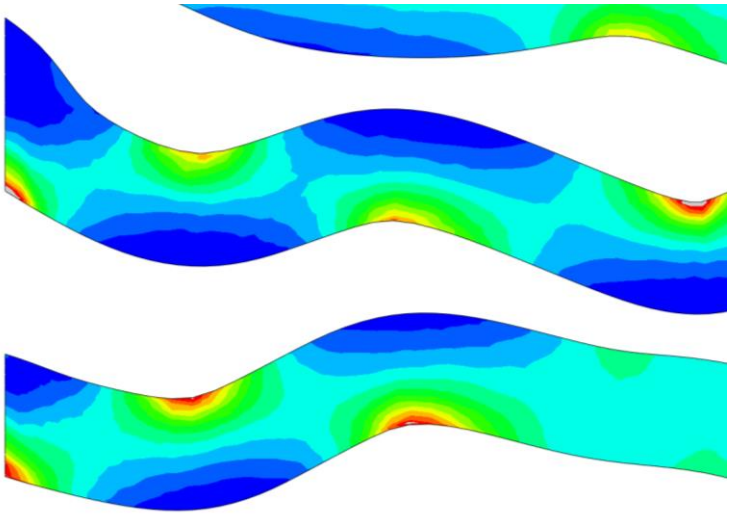

Figure 61: Magnified view of the stress patterns in the axon cylindrical faces, first row

Figure 62 shows the von Mises stress results in the cylindrical axon faces on the second row of axons in the finite element model. The model is oriented with the positive x-Axis pointed into the page.

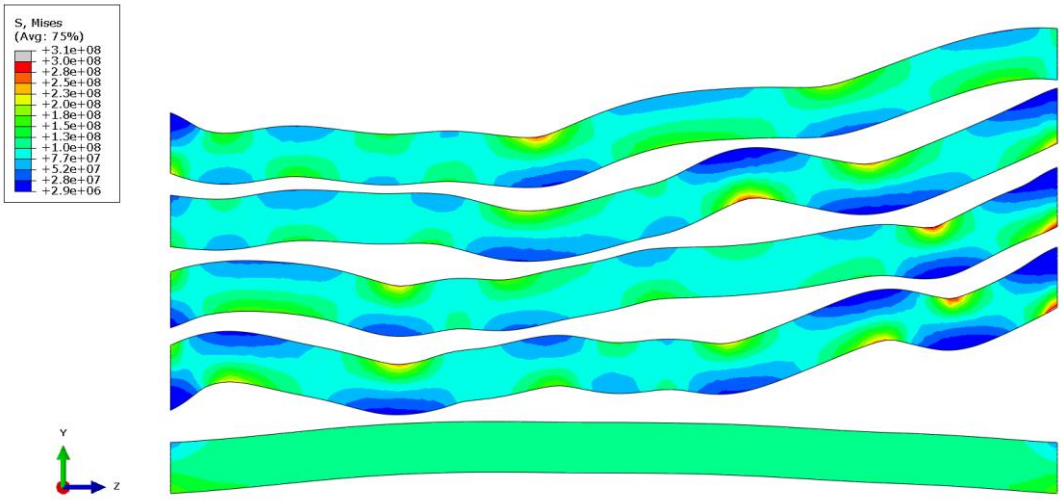

Figure 62: von Mises stresses seen in the cylindrical axon faces, positive x-axis pointed into the page.

Figure 63 shows a magnified view of the cylindrical axon surfaces. Bending stress patterns can be seen on the axon surfaces. The maximum stresses in the model occur at the concave regions in the undulated axon path.

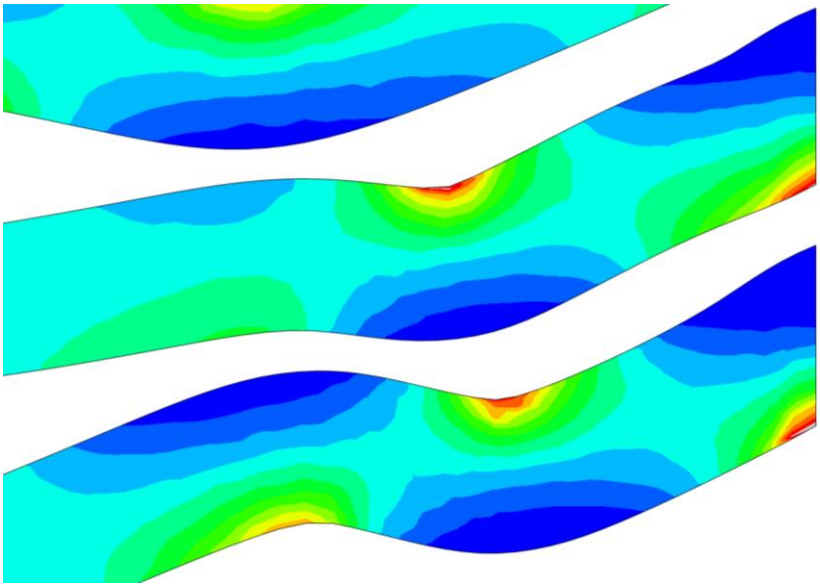

Figure 63: Magnified view of the stress patterns in the axon cylindrical faces, second row

Figure 64 and **Figure 65** show the stress fields measured in the ECM. These figures are provided for reference and do not yield accurate stress results due to the coarse mesh assignment. The figures are provided to give the reader an idea of how stresses propagate in the ECM.

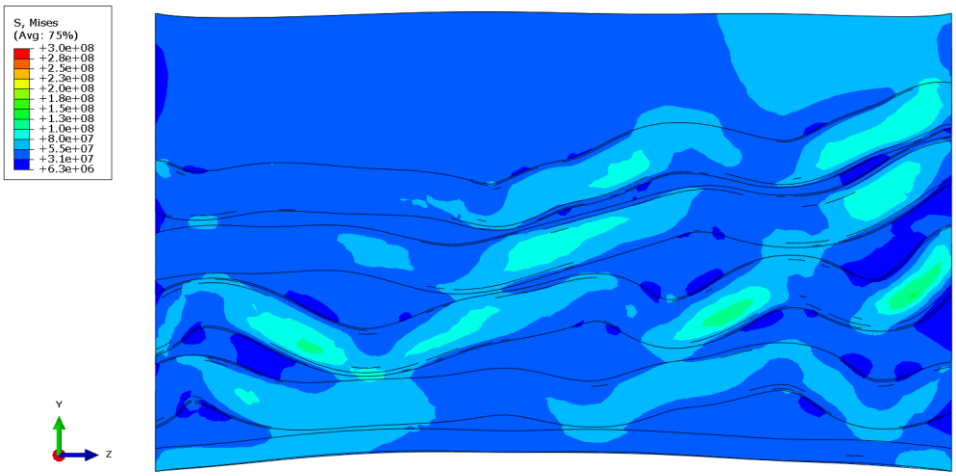

Figure 64:Stress fields in the ECM provided for reference, positive x-axis pointed into the page.

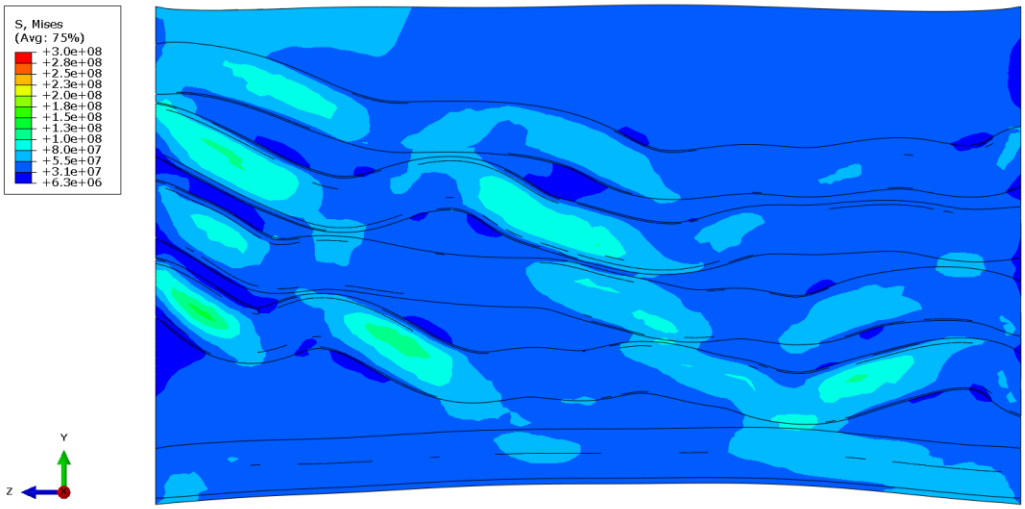

Figure 65: Stress fields in the ECM provided for reference, positive x-axis pointed out of the page.

Figure 66 shows the peak stress found in the model. The peak stresses at the ends of the axons are caused by the kinematic coupling assignments axon faces. The kinematic coupling does not allow for the assigned nodes to interact with the surrounding material or react to external forces. The nodes at the kinematically coupled regions are effectively

fixed in position for the entirety of the load step. The nodes outside of the kinematic couple can react to the applied displacement, while the tied nodes are fully fixed in space. This is not a real stress and is ignored in this analysis.

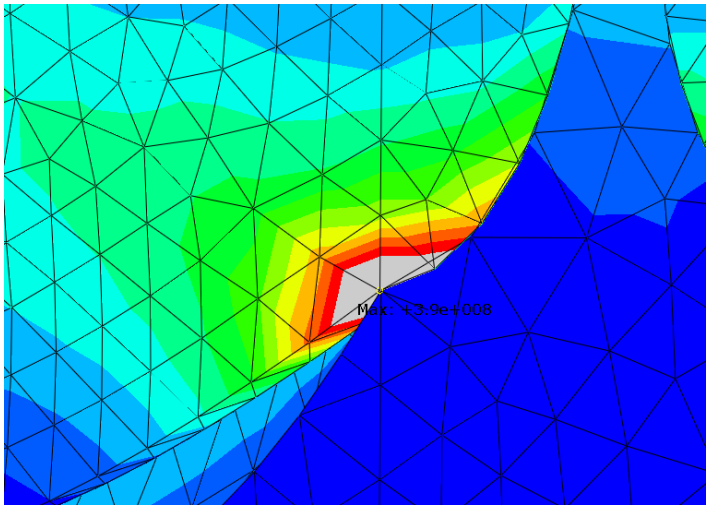

Figure 66: Maximum stress from the nodal proximity to the applied boundary condition.

Disregarding the stresses caused by the applied boundary conditions, the maximum stresses are found in the regions of high undulation in the axon paths. Specifically, the regions with a concave geometry cause a high tensile strain in the axon material. **Figure 67** shows the maximum von Mises stress found in the finite element model, with a value of 340 Pa.

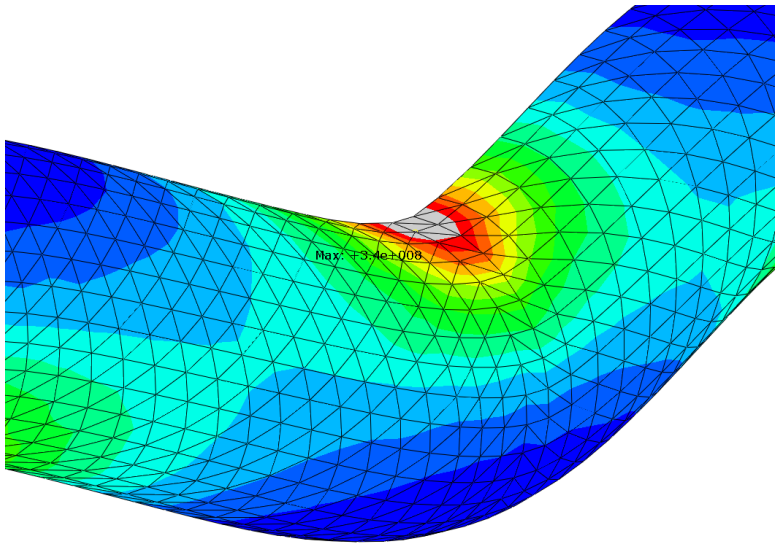

Figure 67: Maximum von Mises stress measured in concave regions of the undulated axons.

Following the trends of sub-models 1 and 2, the axons and ECM separated as both reacted to the tensile load. This is due to the difference in material properties between the axons and ECM. **Figure 68** shows the gaps created between the axons and ECM in the sub-model 3 results.

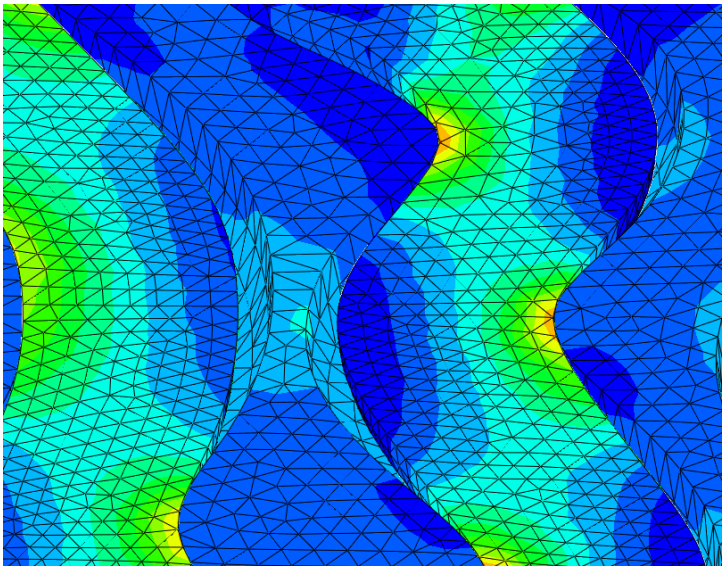

Figure 68: Gaps found between axons and ECM in sub-model 3 results.

Direct comparisons to the other two results will be made later in the report, but as seen in the other two sub-models, bending stresses were still prevalent in the axons as they were subjected to a tensile load. The bending stresses occur at inflection points in the axon undulation paths. The highest stresses measured occur at the concave regions in the axon paths. The single oligodendrocyte seems to distribute the stresses throughout the axons, as the axons have even stress distributions on the outer diameter, but significant peak stresses are seen at regions of high tortuosity. **Figure 69** shows a magnified view of a region with multiple peak stresses.

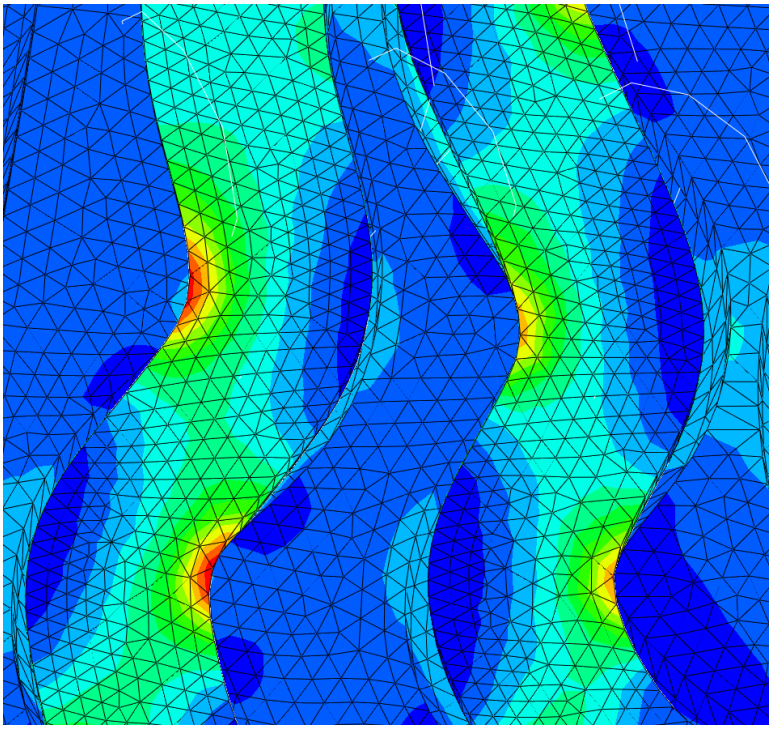

Figure 69: Peak Stresses measured in the regions of high undulation found in sub-model 3.

5.4 Discussion of All Results

All three conditions detailed how stresses are distributed and how the axons react to an external uniaxial tensile load. The axons in all three conditions experienced high stresses

around the concave regions of high undulation – which is expected with a stress concentration at the tight radius. The initial peak stresses in all models represent singular nodes that are reacting to a large displacement in the proximity of a fixed boundary condition. These regions are to be ignored and do not represent accurate stresses in a real-life scenario. Inside of the corpus callosum, the axons will not be fixed in all degrees of freedom and will be able to distribute stresses accordingly. The von Mises stress results in the central regions of the model are a better representation of a real scenario.

Under a uniaxial tension, the models show that axons will experience stresses from both tension and bending. Through laboratory testing it has been proven that the primary mechanism behind traumatic brain injury is axonal failure. Research done on axonal injury has focused on characterizing the tensile and shear properties in axons. Tensile stress regions conditions can be seen reaching up to 130 Pa in condition 1, 130 Pa in condition 2, and 150 Pa in condition 3. Conditions 1 and 2 have lower stress regions in the bottom axons, while condition 3 has an evenly distributed stress throughout. **Figure 70** compares the tensile stresses between the three sub-models with the axon that follows a straight trajectory.

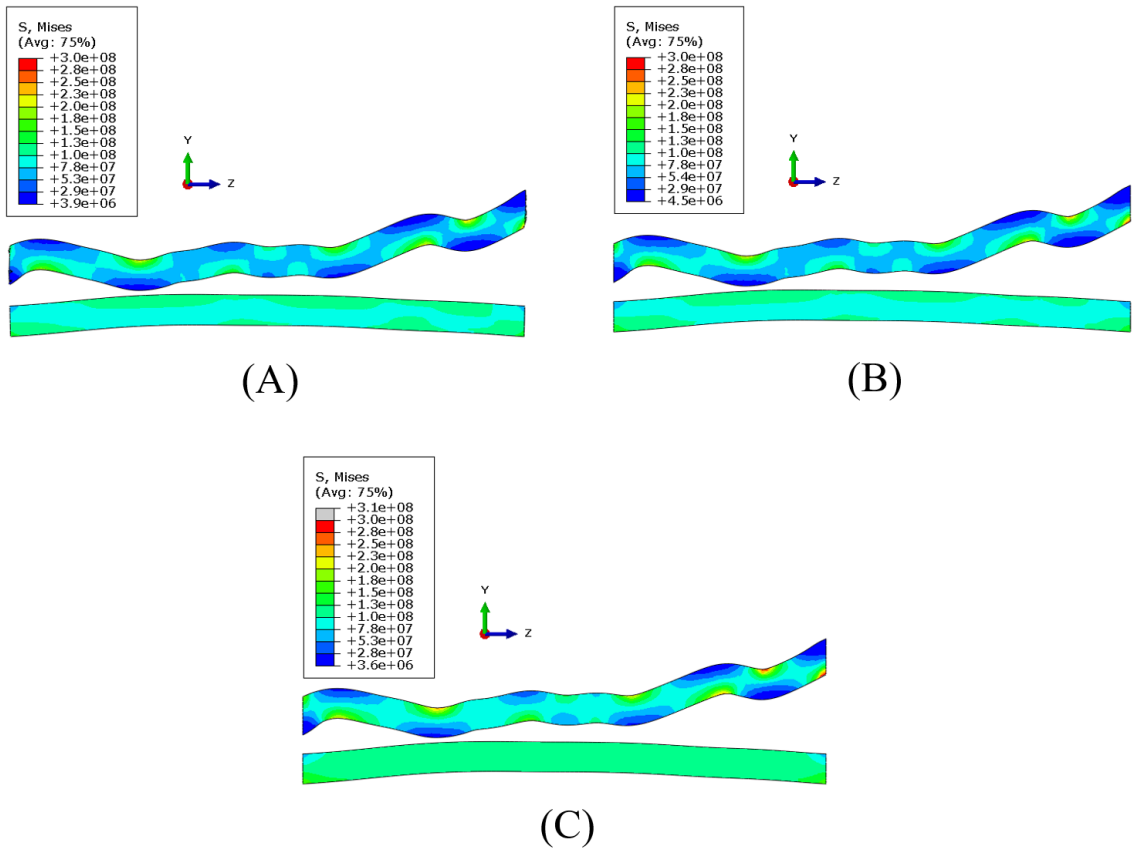

Figure 70: Comparison of tensile stresses between sub-model 1 (A) sub-model 2 (B), and sub-model 3 (C).

The models with the oligodendrocyte representations added a few areas in the axons where stresses were higher due to the oligodendrocyte interacting with the outer diameter of the axons. The maximum von Mises axonal stress (ignoring the singular elements) recorded in condition 1 was equal to 320 Pa, while the maximum stress in conditions 2 and 3 were 310 Pa and 340 Pa, respectively. The maximum stress in condition 2 is slightly lower than in condition 1 and the axon stresses are more uniformly distributed. Condition 3 has higher peak stresses than conditions 1 and 2, with higher mean stresses than both models. Condition 3 also yields more stresses in the undulated regions as compared to the other two conditions. **Figure 71** shows a direct comparison between all three conditions.

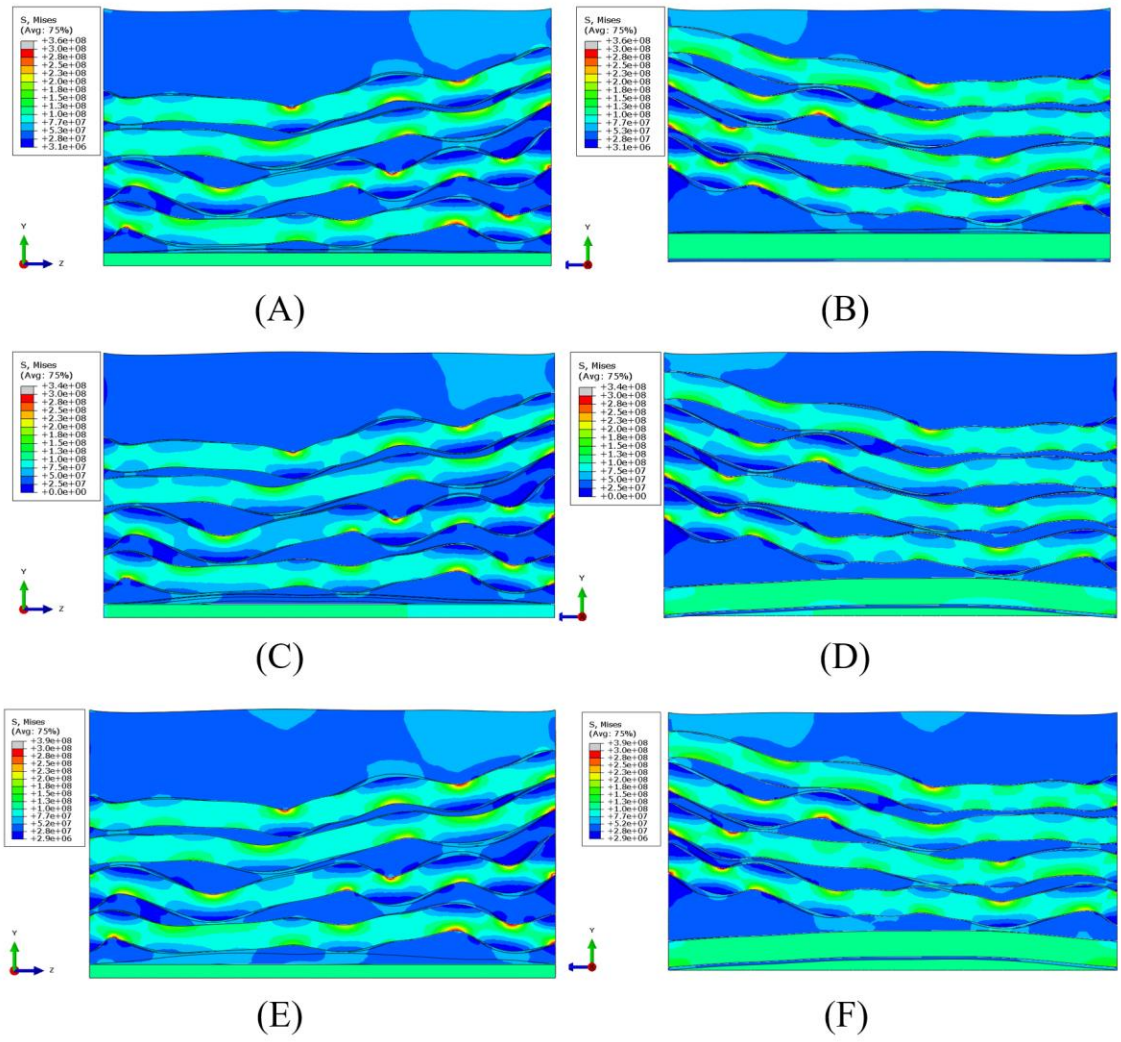

Figure 71: Direct comparison between stress contours in sub-model 1 (A, B) sub-model 2 (C, D), and sub-model 3 (E, F).

The stress contours seen in the three sub-models suggest that the oligodendrocytes aid in distributing stresses through the axons. The oligodendrocyte ties allow for the stresses to be transferred directly into another region of the axon. The stresses found in Condition 3 differ from condition 2 because the single oligodendrocyte effectively ties the center and two end regions together, whereas the oligodendrocytes in condition only tied surrounding axons to each other. Condition 3 allows for a stress/disturbance at one end of the axon to be directly distributed throughout the single axon and other axons around it. The axons in

condition 2 were able to distribute stresses short distances between surrounding axons but were unable to distribute stresses along the entirety of the axon.

All three loading conditions highlighted regions where significant bending stresses can occur. **Figure 72** gives a side-by-side view of bending forces found in a beam and stress contours that indicate the presence of bending stresses in the axons.

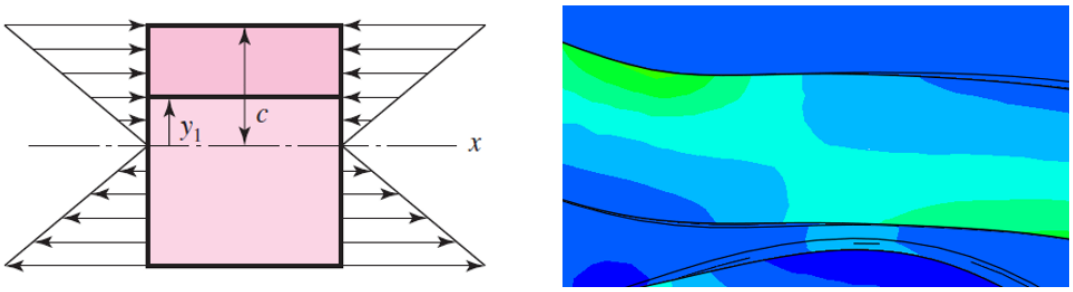

Figure 72: Diagram of bending forces in a beam versus stresses seen in an axon in the finite element model [23].

Under a repeated tensile load, the region is going to experience cyclic loading with no stress reversal. If a cyclic compressive and tensile force is present, then a reversed stress condition is applied to the system. Depending on the magnitude of the cyclic stress in both stress conditions, the axons could potentially suffer from fatigue damage [22, 37]. The magnitude of the stress required for fatigue damage to occur has yet to be determined, as fully reversed loading can drastically change the fatigue life of the axon. Fatigue damage brings a significant risk for axon failure under high strain and cyclic tensile/compressive loading. Low cycle fatigue is a risk if the magnitude of the loading is large enough.

Traumatic events such as a large and sudden impact are known to cause diffuse axonal injury (DAI), but the mechanics behind cumulative damage is still unknown. DAI will destroy axons over a very short period (within milliseconds), while repeated stresses can

take anywhere from tens to millions of cycles before failure. Like ductile materials, hyperelastic materials also suffer from low and high cycle fatigue [22]. The magnitude of the bending stress will largely depend on the geometry of the axons – which is mostly random. Differences between in brain mass and load direction for each individual also play a large part in damaging the cerebral region [30]. More research is required to investigate the possibility of axon fatigue, as many scenarios can drastically change the fatigue life.

6.0 Chapter 6: Conclusions

The finite element analysis performed successfully demonstrated axonal stress propagation under an applied uniaxial tensile strain. The FE model differed from previous efforts with implementation of non-affine kinematics and oligodendrocytes. Non-affine kinematics allowed for the axons to act independently of the ECM using frictionless contact conditions. The ECM and axons were still able to interact with each other, but the axon motion was not fully dictated by the surrounding ECM.

Three sub-models were generated, each with unique conditions. The first condition used a purely non-affine model for the sole purpose of monitoring stresses in the axons subjected to a uniaxial tensile strain. The second and third sub-models incorporated simple representations of oligodendrocytes, with the former model using a grid of 25 oligodendrocytes and the latter using a single oligodendrocyte. Both oligodendrocyte sub-models showed that the oligodendrocytes act as a supporting scaffold for axons. This effort only detailed two oligodendrocyte configurations, but other configurations can be applied to fully understand the supporting effect that oligodendrocytes have on the surrounding axons.

Tensile stresses are still prevalent for axonal failure, but bending stresses were observed multiple times on all axons in the FE model. The bending stresses occur at all inflection points in the axon paths and can occur multiple times in relatively short distances on axons with high undulation. Bending stresses do not have the same magnitude of the peak stresses in the model, but a potential for a fatigue failure exists if the regions are subjected to repeated loading.

Further work to the FE model would include a full fatigue analysis on the axons and ECM, where the system can be subjected to cyclic tensile stresses of alternating magnitudes. The fatigue life of the system will be decreased if a cyclic tensile and compressive load is applied. The effect of varying tensile and compressive stress magnitudes can be studied. Along with varying magnitudes of the applied loads, varying degrees of axon undulation and oligodendrocyte configurations will further support this analysis. Axonal fatigue further supports the idea that axons can suffer from cumulative damage.

Bibliography

[1] Pan, Yi, Daniel Sullivan, David I. Shreiber, and Assimina A. Pelegri. “Finite Element Modeling of CNS White Matter Kinematics: Use of a 3D RVE to Determine Material Properties.” *Biomechanics* 1 (2013): 19. https://doi.org/10.3389/fbioe.2013.00019.

[2] Meaney, D. F. “Relationship between Structural Modeling and Hyperelastic Material Behavior: Application to CNS White Matter.” Biomechanics and Modeling in Mechanobiology; Dordrecht 1, no. 4 (April 2003): 279–93. http://dx.doi.org.proxy.libraries.rutgers.edu/10.1007/s10237-002-0020-1.

[3] Karami et al., G., N. Grundman, N. Abolfathi, A. Naik, and M. Ziejewski. “A Micromechanical Hyperelastic Modeling of Brain White Matter under Large Deformation.” Journal of the Mechanical Behavior of Biomedical Materials 2, no. 3 (July 2009): 243–54. https://doi.org/10.1016/j.jmbbm.2008.08.003.

[4] Yousefsani et al., S.A, Farahmand, F. Shamloo, A. "Micromechanical Modeling of Brain White Matter Using Embedded Element Technique"

[5] M. O’Toole, P. Lamoureux, and K. E. Miller, “A Physical Model of Axonal Elongation: Force, Viscosity, and Adhesions Govern the Mode of Outgrowth,” Biophys J, vol. 94, no. 7, pp. 2610–2620, Apr. 2008.

[6] Y. Pan, D. I. Shreiber, and A. A. Pelegri, “A Transition Model for Finite Element Simulation of Kinematics of Central Nervous System White Matter,” IEEE Transactions on Biomedical Engineering, vol. 58, no. 12, pp. 3443–3446, Dec. 2011.

[7] Y. Pan, L. Iorga, and A. A. Pelegri, “Analysis of 3D random chopped fiber reinforced composites using FEM and random sequential adsorption,” Computational Materials Science, vol. 43, no. 3, pp. 450–461, Sep. 2008.

[8] S. Singh, A. A. Pelegri, and D. I. Shreiber, “Characterization of the three-dimensional kinematic behavior of axons in central nervous system white matter,” Biomech Model Mechanobiol, pp. 1–13, Apr. 2015.

[9] K. B. Arbogast and S. S. Margulies, “Material characterization of the brainstem from oscillatory shear tests,” Journal of Biomechanics, vol. 31, no. 9, pp. 801–807, Sep. 1998.

[10] D. Bray, “Axonal growth in response to experimentally applied mechanical tension,” Developmental Biology, vol. 102, no. 2, pp. 379–389, Apr. 1984.

[11] K. Miller and K. Chinzei, “Mechanical properties of brain tissue in tension,” Journal of Biomechanics, vol. 35, no. 4, pp. 483–490, Apr. 2002.

[12] A. C. Bain, D. I. Shreiber, and D. F. Meaney, “Modeling of Microstructural Kinematics During Simple Elongation of Central Nervous System Tissue,” J Biomech Eng, vol. 125, no. 6, pp. 798–804, Jan. 2004.

[13] Y. Assaf, T. Blumenfeld-Katzir, Y. Yovel, and P. J. Basser, “Axcaliber: A method for measuring axon diameter distribution from diffusion MRI,” Magnetic Resonance in Medicine, vol. 59, no. 6, pp. 1347–1354, 2008.

[14] S. Javid, A. Rezaei, and G. Karami et al., “A micromechanical procedure for viscoelastic characterization of the axons and ECM of the brainstem,” Journal of the Mechanical Behavior of Biomedical Materials, vol. 30, pp. 290–299, Feb. 2014.

[15] Abaqus 6.14 Docmentation

[16] A. W. Holle et al., “Cell–Extracellular Matrix Mechanobiology: Forceful Tools and Emerging Needs for Basic and Translational Research,” Nano Letters, vol. 18, no. 1, pp. 1–8, Jan. 2018.

[17] D. I. Shreiber, H. Hao, and R. A. Elias, “Probing the influence of myelin and glia on the tensile properties of the spinal cord,” Biomechanics and Modeling in Mechanobiology; Dordrecht, vol. 8, no. 4, pp. 311–21, Aug. 2009.

[18] Bergström, J. (2015). Mechanics of solid polymers. Amsterdam [etc.]: Elsevier/William Andrew.

[19] P. K. Stys, “Anoxic and Ischemic Injury of Myelinated Axons in CNS White Matter: From Mechanistic Concepts to Therapeutics,” J Cereb Blood Flow Metab, vol. 18, no. 1, pp. 2–25, Jan. 1998.

[20] N. J. Allen and B. A. Barres, “Neuroscience: Glia — more than just brain glue,” Nature, vol. 457, no. 7230, pp. 675–677, Feb. 2009.

[21] M. Simons and K.-A. Nave, “Oligodendrocytes: Myelination and Axonal Support,” Cold Spring Harb Perspect Biol, vol. 8, no. 1, p. a020479, Jan. 2016.

[22] G. Ayoub, F. Zaïri, M. Naït-Abdelaziz, and J. M. Gloaguen, “Modeling the low-cycle fatigue behavior of visco-hyperelastic elastomeric materials using a new network alteration theory: Application to styrene-butadiene rubber,” Journal of the Mechanics and Physics of Solids, vol. 59, no. 2, pp. 473–495, Feb. 2011.

[23] Budynas, Richard G, J K. Nisbett, and Joseph E. Shigley. Shigley's Mechanical Engineering Design. New York: McGraw-Hill, 2011. Print.

[24] D. Shreiber, “Experimental and computational modeling of traumatic brain injury: In vivo thresholds for mechanical disruption of the blood-brain barrier,” ProQuest Dissertations Publishing, 1998.

[25] A. C. Bain and D. F. Meaney, “Tissue-level thresholds for axonal damage in an experimental model of central nervous system white matter injury,” J Biomech Eng, vol. 122, no. 6, pp. 615–622, Dec. 2000.

[26] R. J. H. Cloots, H. M. T. Gervaise, J. A. W. van Dommelen, and M. G. D. Geers, “Biomechanics of Traumatic Brain Injury: Influences of the Morphologic Heterogeneities of the Cerebral Cortex,” Ann Biomed Eng, vol. 36, no. 7, p. 1203, May 2008.

[27] R. J. H. Cloots, J. a. W. van Dommelen, T. Nyberg, S. Kleiven, and M. G. D. Geers, "Micromechanics of diffuse axonal injury: influence of axonal orientation and anisotropy," Biomech Model Mechanobiol, vol. 10, no. 3, pp. 413–422, Jun. 2011.

[28] J. Ho and S. Kleiven, "Dynamic response of the brain with vasculature: A three-dimensional computational study," Journal of Biomechanics, vol. 40, no. 13, pp. 3006–3012, Jan. 2007.

[29] T. J. Horgan and M. D. Gilchrist, "The creation of three-dimensional finite element models for simulating head impact biomechanics," vol. 8, no. 4, p. 14.

[30] S. Kleiven, "Evaluation of head injury criteria using a finite element model validated against experiments on localized brain motion, intracerebral acceleration, and intracranial pressure," International Journal of Crashworthiness, vol. 11, no. 1, pp. 65–79, Jan. 2006.

[31] K. Miller, K. Chinzei, G. Orssengo, and P. Bednarz, "Mechanical properties of brain tissue in-vivo: experiment and computer simulation," J Biomech, vol. 33, no. 11, pp. 1369–1376, Nov. 2000.

[32] A. Post, B. Hoshizaki, and M. D. Gilchrist, "Finite element analysis of the effect of loading curve shape on brain injury predictors," J Biomech, vol. 45, no. 4, pp. 679–683, Feb. 2012.

[33] S. A. Tabatabaei, S. V. Lomov, and I. Verpoest, "Assessment of embedded element technique in meso-FE modelling of fibre reinforced composites," Composite Structures, vol. 107, pp. 436–446, Jan. 2014.

[34] F. Velardi, F. Fraternali, and M. Angelillo, "Anisotropic constitutive equations and experimental tensile behavior of brain tissue," Biomech Model Mechanobiol, vol. 5, no. 1, pp. 53–61, Mar. 2006.

[35] K. B. Arbogast and S. S. Margulies, "A fiber-reinforced composite model of the viscoelastic behavior of the brainstem in shear," Journal of Biomechanics, vol. 32, no. 8, pp. 865–870, Aug. 1999.

[36] Dill, E. (2012). The finite element method for mechanics of solids with ANSYS applications. Boca Raton, FL: CRC.

[37] E. Verron, G. Chagnon, and J.-B. Le Cam, "Hyperelasticity with volumetric damage," in Sixth European Conference on Constitutive Models for Rubber (ECCMR VI), Dresde, Germany, 2009.